INVITED PAPER

Continuum Robots for Medical Interventions

This article provides a unified summary of the state of the art of continuum robot architectures with respect to design for specific clinical applications.

By Pierre E. Dupont, *Fellow IEEE*, Nabil Simaan, *Fellow IEEE*,
Howie Choset, *Fellow IEEE*, and Caleb Rucker, *Member IEEE*

ABSTRACT | Continuum robots are not constructed with discrete joints but, instead, change shape and position their tip by flexing along their entire length. Their narrow curvilinear shape makes them well suited to passing through body lumens, natural orifices, or small surgical incisions to perform minimally invasive procedures. Modeling and controlling these robots are, however, substantially more complex than traditional robots comprised of rigid links connected by discrete joints. Furthermore, there are many approaches to achieving robot flexure. Each presents its own design and modeling challenges, and to date, each has been pursued largely independently of the others. This article attempts to provide a unified summary of the state of the art of continuum robot architectures with respect to design for specific clinical applications. It also describes a unifying framework for modeling and controlling these systems while additionally explaining the elements unique to each architecture. The major research accomplishments are described for each topic and directions for the future progress needed to achieve widespread clinical use are identified.

KEYWORDS | Concentric tube robots; continuum robots; medical robots; multibackbone robots; tendon actuation.

I. INTRODUCTION

Continuum robots find wide application in medicine since they can be designed to achieve a high ratio of length to width making them well suited to minimally invasive and endoluminal medical interventions. These robots are defined as being comprised of deformable elongate elements forming a smoothly curving structure whose shape is controlled primarily through flexure, relative translation, linear extension, and twisting of the elongate elements. These continuously deforming structures have an infinite number of degrees of freedom, but the number of kinematic inputs to control their shape is typically small. While continuum robots lack discrete joints, their curvilinear shape can be approximated by snake-like robot designs possessing large numbers of serially connected discrete joints. Continuum robots taken together with such snake-like discrete-jointed designs comprise the set of kinematically hyperredundant robots. While discrete-jointed designs are not continuum robots, they are a design alternative in medical applications and so are included here.

A. Design Classification

Continuum robot designs can be classified predominantly by the method of shape control. While five major design classes are defined below, many hybrid designs are possible that incorporate aspects of several of the design classes.

1) Tendon-Actuated Designs: Shape control of the structural elongate elements of continuum robots is often achieved using additional deformation-inducing elongate elements specifically included to apply forces and torques to the structural elongate elements. Tendon-based designs, as shown in Fig. 1(a) and (b), are the most popular method of shape control. Here, the structural elongate element is a tube that is relatively stiff longitudinally but flexurally

---

Manuscript received October 15, 2021; revised December 9, 2021; accepted December 28, 2021. Date of publication February 8, 2022; date of current version June 20, 2022. The work of Pierre E. Dupont was supported in part by the NIH under Grant R01NS099207 and Grant R01HL124020. The work of Nabil Simaan was supported in part by NSF under Grant 1734461. The work of Howie Choset was supported in part by the U.S. Army under Contract W81XWH-19-C0083 and Contract W81XWH-19-C0101. The work of Caleb Rucker was supported in part by NSF under Grant IIS-1652588. *(Corresponding author: Pierre E. Dupont.)*

Pierre E. Dupont is with the Department of Cardiovascular Surgery, Boston Children's Hospital, Harvard Medical School, Boston, MA 02115 USA (e-mail: pierre.dupont@childrens.harvard.edu).

Nabil Simaan is with the Department of Mechanical Engineering, the Department of Computer Science, and the Department of Otolaryngology, Vanderbilt University, Nashville, TN 37235 USA (e-mail: nabil.simaan@vanderbilt.edu).

Howie Choset is with the Mechanical Engineering Department, the Biomedical Engineering Department, and the Robotics Institute, Carnegie Mellon, Pittsburgh, PA 15213 USA (e-mail: choset@andrew.cmu.edu).

Caleb Rucker is with the Department of Mechanical, Aerospace, and Biomedical Engineering, The University of Tennessee, Knoxville, TN 37996 USA (e-mail: caleb.rucker@utk.edu).

Digital Object Identifier 10.1109/JPROC.2022.3141338

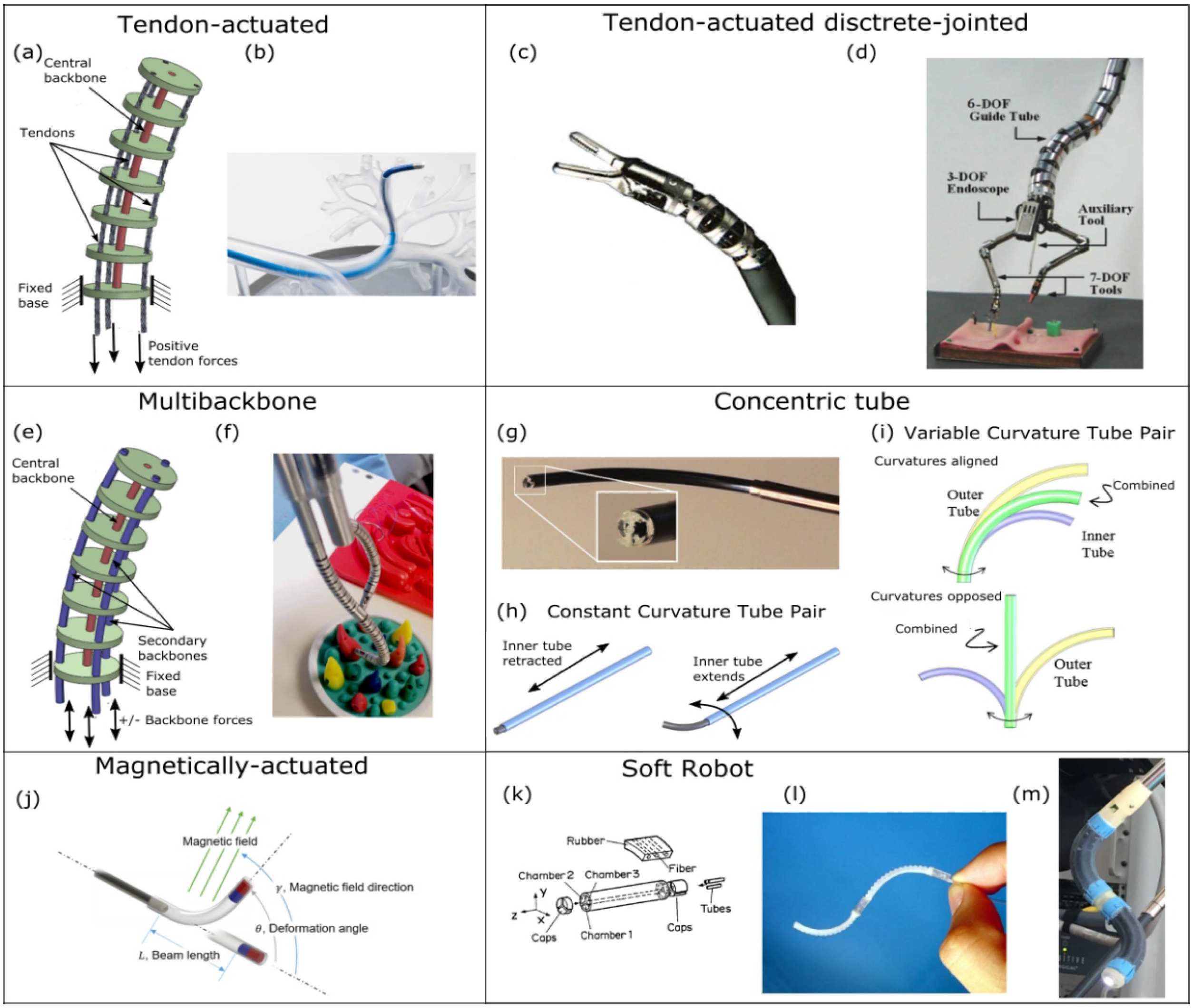

Fig. 1. *Continuum robot design classification. (a) In tendon-actuated designs, tendons run through channels in disks attached to the central backbone. In many clinical applications, the central backbone and disks are replaced by a tube with small lumens for each tendon plus a larger central lumen as shown in (b). (b) Tendon-actuated Monarch® robotic endoscope by Auris™ Health, Inc. © Auris Health, Inc. Reproduced with permission. (c) Intuitive Surgical's 5-mm-diameter laparoscopic instrument [12]. (d) Steerable sheath of Samsung's NOTES robot [13]. (e) Multibackbone actuation replaces the tendons with secondary backbones that can exert both tensile and compressive forces on the structure. (f) Multibackbone arms of the Enos single-port robot by Titan Medical, Inc. [14]. (g) Concentric tube robot comprised of telescoping sections of either constant or variable curvature [15]. (h) Constant curvature section is comprised of a precurved inner tube that conforms to the shape of a stiffer outer tube when retracted. (i) Variable curvature section is comprised of tube pairs of approximately equal stiffness and precurvature. Relative rotation of the combined tubes varies curvature from the maximum value to approximately straight. (j) Magnetically actuated catheter. Magnetic dipole embedded in robot tip experiences a torque causing it to move toward alignment with an externally generated magnetic field (from [10]). (k) Soft robots use pneumatic actuation. Here, the sheath is comprised of three internal chambers that can be independently pressurized. Acting as tensile tendons, the pressurized chambers cause the robot to bend (from [16]). (l) Soft multisegment catheter (from [17]). (m) Stiff-flop soft medical robot [18].*

compliant. Between one and four tendons, fixed at the distal end, run along the length of the tube offset from the tube's neutral axis.

Tension applied to tendons at the proximal end of the tube generates bending along its length. Since the tendons are highly compliant in bending, the overall flexural stiffness is that of the tube. Common design variations include varying tube stiffness along the length, so as to localize bending in a specific region, e.g., at the tip, as well as concatenating bendable sections, so as to produce more complicated curves, e.g., a two-section tube capable of an "S" curve [1].

2) Tendon-Actuated Discrete-Jointed Designs: Tendon actuation is also used to control (noncontinuum) hyper-redundant discrete-jointed designs, such as the examples shown in Fig. 1(c) and (d). These designs can potentially offer higher stiffness and reduced manufacturing cost compared to tendon-actuated continuum designs.

3) Multibackbone Designs: In these designs (Fig. 1(e) and (f)), elongate elements act as both structural and deformation-inducing components. For example, in the "multibackbone" design of Fig. 1(e), a central element acts as a purely structural component, while the surrounding elements [tubes or flexurally stiff wires replacing the tendons of Fig. 1(a)] are both structural and deformation-inducing through tensile and compressive loads applied at the base [2]. Such designs can provide greater stiffness than tendon actuation.

4) Concentric Tube Designs: The tendon-actuated and multibackbone designs of Fig. 1(a)–(f) rely on the elongate elements being attached to each other at their distal ends. Another class of continuum robots forgoes this rigid connection and substitutes precurvature of the individual elements as a means of inducing bending in the other elements and so controlling overall shape. These designs are known as concentric tube robots [3], [4]. As shown in Fig. 1(g), they are comprised of a set of precurved tubes that are inserted inside each other. The overall shape of the assembled tubes is controlled by translating and rotating the tubes with respect to each other at their proximal ends. These robots are typically constructed as telescoping sections of either constant or varying curvature [3], [5]. These section types are defined in Fig. 1(h) and (i). Recent variations on this design strategy include arranging some or all of the precurved elements eccentrically [6]–[8].

5) Magnetically Actuated Designs: In the designs described above, shape control is achieved by applying displacements or forces/torques at the proximal end of the robot. This makes these robots much slimmer along their length and much easier to sterilize in comparison with robot designs that locate discrete joints and motors along their length. An alternative design strategy that can further reduce robot diameter is to control robot shape using magnetic fields generated external to the patient [see Fig. 1(j)]. These fields can be created using electromagnets [9], permanent magnets [10], or even an MRI scanner [11]. This approach is well suited for medical applications requiring particularly long robots, e.g., 1 m, as in some endovascular procedures. The external magnetic field acts on ferromagnetic material in the tip of the robot to bend it in the desired direction, while its inserted length is mechanically controlled at its base.

6) Soft Robot Designs: The structural and deformation-inducing elongate elements of the continuum robots described above are typically composed of metals, polymers, and their combinations. An alternative approach is to construct the robot entirely from rubbery materials and accomplish shape change by incorporating pneumatic or hydraulic chambers within the elongate elements. Such designs are called "soft robots" and comprise a subset of continuum robots. The design strategies of these robots can parallel those of nonsoft continuum robots. For example, Fig. 1(k) shows the soft analog of tendon/multibackbone actuation. The extension and bending of the robot are controlled via relative pressurization of the three internal chambers. Multisection designs have been produced, as shown in Fig. 1(l) and (m). Hybrid designs are also possible, which combine the actuation methods and materials of soft and nonsoft continuum robots.

B. History and Seminal Results for Design Families

Manual medical instruments based on many of the designs described above predate their robotic versions and still outnumber them today. The major clinical motivation has been to add steerability to endoscopes and catheters. Patents dating to the 1920s for endoscopes [19] and the 1950s for catheters [20] describe tendon-actuated devices based on both continuum and snake-like designs [21]. A 1941 patent describes using tendons sufficiently stiff to both push and pull as in multibackbone designs [22].

In a steerable catheter patent filed in 1966 [23], tendon-actuation is suggested to be a favorable alternative to using combinations of precurved tubes and magnetic steering using moveable magnets outside the body. Consequently, while balloon catheters date back to the 1960s [24], soft robots appear to be the only continuum design not initially introduced or contemplated as a manually steerable medical device.

Manual shape control is accomplished using knobs and sliders mounted on the instrument handle. The large strains and the significant friction between sliding and rotating components in these designs produce substantial hysteresis that the operator must compensate for using image-based feedback. For simple steering motions, mastery of manual control can be achieved through practice. Nevertheless, instrument steering continues to consume some fraction of mental bandwidth, may necessitate several operators to maintain control of all degrees of freedom, and can require a minimum number of cases per year to maintain proficiency.

Robotics can improve upon manual instruments by providing intuitive or autonomous control of larger numbers of degrees of freedom by a single operator, improving operator ergonomics, automatically compensating for hysteresis and friction, and enabling the integration of preoperative image-based planning. Thus, the major contribution of the robotics research community, as summarized below, has not been to invent the continuum and snake-like mechanisms but rather to formalize each design and create the tools needed to implement this robotic functionality.

1) Tendon-Actuated Designs: The seminal work on the modeling and control of tendon-actuated catheters was done by Camarillo [25] as his Ph.D. thesis and published in [26] and [27] under funding provided by Hansen Medical, Inc., which was developing an electrophysiology catheter for performing cardiac ablations. While Hansen Medical ultimately did not succeed commercially, their IP was acquired by Auris Health, Inc. (now owned by J&J) and is currently being applied to airway endoscopy for performing peripheral lung biopsies [28].

2) Tendon-Actuated Discrete-Jointed Designs: Several of these noncontinuum robots have been used clinically. For example, Intuitive Surgical's 5-mm-diameter instruments employ a serial arrangement of revolute joints actuated by tendons to approximate the wrist motion of their 8-mm-diameter instruments [12]. Degani *et al.* [29] introduced a novel design comprised of two concentrically arranged snakes. Each snake is composed of cylindrical links connected by spherical joints. Three tendons run through the outer snake and one through the inner snake. When the tendons for either snake are pulled tight, friction between the links causes the snake to become stiff in its current shape. When loose, the snake is deformable. The two snakes can be extended along any curve in 3-D by tensioning the inner snake while extending the outer snake and curving its extended tip in the desired direction. The outer snake tendons are then tightened in that shape, and the inner snake makes a limp and extended to the tip of the outer snake. The process is then repeated. This design was employed as a steerable robotic sheath by MedRobotics, Inc. and combined with two manually actuated arms running parallel to and external to the sheath [see Fig. 2(a)]. These systems were approved for use in transoral and transanal procedures and were used clinically up until a few years ago [30].

3) Multibackbone Designs: The seminal work on this design was performed at Johns Hopkins University by Simaan during his postdoctoral studies with R. H. Taylor. They developed a system similar to Fig. 2(b) for transoral surgery [31]. Simaan's motivation for using multiple backbones instead of tendons was to create stiffer and stronger designs while also promoting design miniaturization since push–pull designs require fewer actuation lines than pull-only designs. This technology was used in the early development stages of the Titan Medical, Inc. SPORT system for single-port access surgery [14].

4) Concentric Tube Designs: The practice of using combinations of curved and straight tubes and wires to navigate bifurcations in the vasculature is a staple of cardiology. This practice uses predominantly the approach of Fig. 1(h) in which the overlapping portion of a more compliant elongate element conforms to the shape of a stiffer element. This method has also been used in needle steering [32]. The varying curvature approach of Fig. 1(e) involving the rotation of two elongate elements of comparable precurvature and flexural stiffness enables active control of flexure similar to tendon-based actuation. The formalization of these concepts as a robot design was proposed independently by two groups in initial papers appearing at the same conference [33], [34]. More complete descriptions of the technology followed in [3], [4], [35], and [36]. Dupont's group at Boston University developed the concept while working on needle-based tools for fetal interventions. The second group, comprised of Okamura, Cowan, Chirikjian, and Webster at Johns Hopkins University, was motivated by applications in endoscopic neurosurgery. The properties of concentric tube robots make them best suited for clinical applications requiring arm diameters of about 2 mm and steerable lengths less than about 10 cm. Current translational efforts are focused on endoscopic robots employing pairs of teleoperated concentric tube robots as the surgeon's arms.

5) Magnetically Actuated Designs: In the last 30 years, several companies (Stereotaxis [37], Magnetecs [38], and Aeon Scientific [39]) have developed magnetic catheters for cardiac electrophysiology procedures. Of the three, only Stereotaxis is still in business. Founded in 1990, it first targeted neurovascular interventions before focusing on the treatment of cardiac arrhythmias. Tunay [40]–[42], while a staff scientist at Stereotaxis, published early work on the modeling of magnetically steerable catheters. More recently, Nelson's group, which has produced fundamental results on medical electromagnetic navigation systems [43], has devoted effort to magnetic catheter control [39], [44].

6) Soft Robot Designs: Some of the earliest examples of soft continuum robots date to [16] [see Fig. 1(k)]. Application of soft designs to medical devices can be traced to Ikuta's work on steerable catheters [17] [see Fig. 1(l)]. In the last decade, there has been an explosion of interest in soft medical robots. While many of the designs are variations on [16], recent work has focused on manufacturing techniques, modeling, and control [45]. To date, little work has been done developing soft continuum robots for specific clinical applications, and there are no soft continuum robots used clinically.

As described above, the major contribution of the robotics research community has been to develop the tools needed to convert continuum devices already employed clinically, either formally or informally, to robotic systems. The remainder of this article summarizes these contributions. Section II discusses robot design and describes how continuum robot design types can be mapped to clinical applications. Section III describes the modeling principles that have been developed for these systems. Section IV covers the control and planning strategies that have been developed for continuum medical robots. Finally, Section V examines open challenges and future applications.

II. DESIGNING MEDICAL ROBOTS USING CONTINUUM ARCHITECTURES

In medical procedures, continuum robots are used to minimize the trauma created in reaching the site of intervention. This may involve reducing the diameter of the surgical corridor passing through healthy tissue, or it may involve passing through body lumens entered percutaneously or through a natural orifice. One measure for

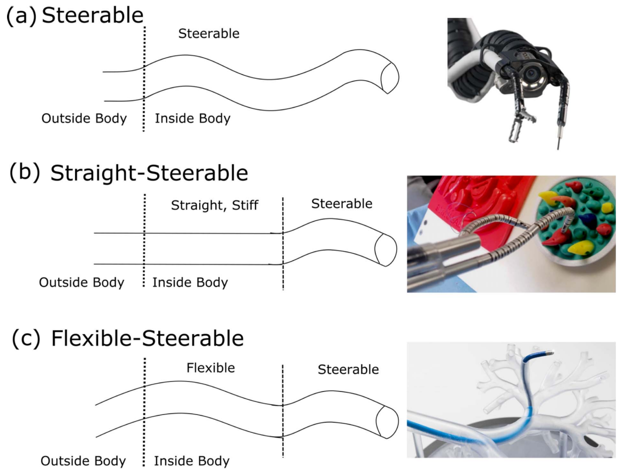

Fig. 2. ***Continuum robot implementations based on slenderness ratio. (a) Steerable system: entire portion of continuum robot inserted inside body is steerable. Used for slenderness ratios of less than about 50. Example: Medrobotics, Inc. Flex robot with steerable sheath [30]. (b) Straight-steerable system: robot is comprised of a straight stiff proximal section with a steerable distal section for slenderness ratios of about 100. Example: Titan Medical, Inc. Enos single-port robot with straight-steerable arms [14]. (c) Continuum robot is comprised of a passive flexible proximal section and a steerable distal section for slenderness ratios of 100 to over 1500 (flexible-steerable). Example: Auris$^{\text{TM}}$ Heath, Inc. Monarch® robotic endoscope [28]. © Auris Health, Inc. Reproduced with permission.***

assessing the invasiveness of a robot is to compute the ratio of its inserted length divided by its diameter with larger ratios equating to less invasiveness. Let us define this quantity as the slenderness ratio, s, which is similar, but not equal to the quantity defined in analyzing the buckling of columns.

As this ratio increases, the flexural tip compliance in a cantilevered configuration grows cubically, and a robot constructed with any of the architectures described here becomes unable to support its own weight. This limitation has led to the three implementations of the medical continuum robot shown in Fig. 2. The first type of Fig. 2(a) (steerable) provides active shape control along its entire inserted length. While this design is the most versatile, it is limited to slenderness ratios less than about 50.

To achieve larger slenderness ratios, it is possible to mount the steerable continuum robot at the distal end of a straight and relatively stiff shaft, as shown in Fig. 2(b) (straight-steerable). This design maintains a slenderness ratio of less than 50 for the steerable portion, while the ratio for the entire inserted length can be on the order of 100. With this concept, however, the robot reaches the interventional site by following a straight path.

To enable intraluminal procedures deep inside the body, the steerable continuum robot can be mounted at the tip of a passive flexible tube, as shown in Fig. 2(c) (flexible-steerable). With this approach, slenderness ratios of 1500 are standard. While the proximal flexible portion conforms to the shape of the surrounding tissue, this interaction is stiff enough to enable the steerable tip to be positioned and oriented inside the lumen.

For all three implementations, the degrees of freedom consist of base insertion/retraction and rotation combined with the degrees of freedom of the steerable portion.

A. Clinical Application Versus Slenderness Ratio

To show how these three designs map into various clinical procedures, Fig. 3 plots the length versus the diameter of standard classes of medical devices and robots.

1) High Slenderness Ratios (Flexible-Steerable Systems): Flexible-steerable designs correspond to steerable catheters, ureterscopes, bronchoscopes, gastroscopes, and bronchoscopes. These devices predate medical robots and were developed as manual endoluminal instruments to provide an alternative to some of the most invasive surgeries. Making these devices robotic does not necessarily add new degrees of freedom nor reduce invasiveness but can facilitate control, integration of planning, and sensing while also providing improved ergonomics.

Steerable endovascular catheters are used for navigating vascular bifurcations, repairing heart valves, and treating cardiac arrhythmias. With typical lengths of up to 1.25 m and diameters ranging from 1 to 5 mm, these devices have slenderness ratios of 200–1250 [46], [47].

Similarly, ureterscopes are used to navigate into the kidneys to break up kidney stones. With lengths of 65–70 cm and diameters of 2.5–3.1 mm, they have a slenderness ratio of 210–280 with a typical steerable tip length of 7 cm [48], [49].

The use of bronchoscopes to perform tumor biopsies in the peripheral lung regions has received interest from the commercial robotics community. Both Intuitive Surgical's Ion System [50] and Auris Health's Monarch platform (Johnson & Johnson) [51] are recently introduced robotic bronchoscopes. While manual systems with comparable diameters and lengths are available (e.g., 3-mm diameter,

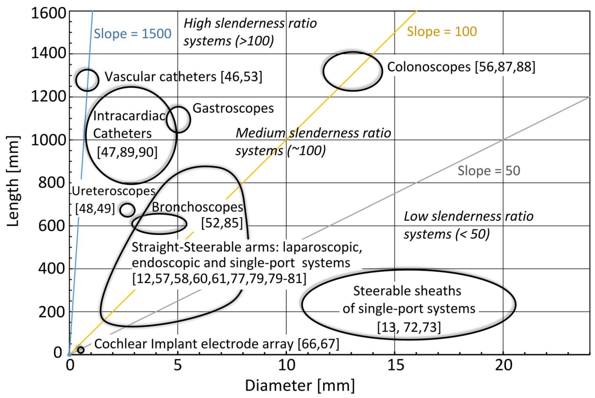

Fig. 3. ***Length versus diameter of standard classes of medical devices and continuum robots.***

60-cm length, slenderness ratio 200 [52]), the robotic systems offer a number of advantages. They provide more degrees of freedom in their steerable tips enabling more reliable navigation to all segments of the lungs. Clinician control of motion through input devices similar to game controllers is easier and enables the endoscope tip to be parked “hands free” in the desired location. Integrated tracking sensors and navigation software make reaching the desired target easier and more repeatable.

Note that there are also high slenderness ratio medical devices that can be viewed as flexible–flexible, meaning that they are entirely passive along their length. For example, most vascular navigation is performed using wires and catheters that are flexible along their entire length but may be curved at the tip. Steering is accomplished using only base insertion, retraction, and rotation. The Corindus, Inc. (Siemens) catheter system implements a robotic version of this approach [53]. Similarly, steering a long needle along a curved path through tissue is often accomplished using a passive needle [54], [55]. These flexible devices may be viewed as continuum robots even though their flexure is produced entirely through reaction forces with the surrounding tissue.

Additional high slenderness ratio devices include gastroscopes for use in the esophagus, stomach, and duodenum and colonoscopes for the inspection, biopsy, and resection of lesions in the colon. While both devices have lengths exceeding 1 m, gastroscopes have smaller diameters (typically 5 mm) yielding a slenderness ratio of about 200. Colonoscopes are larger in diameter (13-mm diameter) and possess slenderness ratios (100) comparable to the straight-steerable systems, as described in the following [56].

2) Medium Slenderness Ratios (Straight-Steerable Systems): Straight-steerable continuum robot designs are often used to replace manual laparoscopic and endoscopic tools that consist of a straight shaft but lack steerability at the tip. These robots typically add degrees of freedom through tip steerability. For example, a key feature of the straight-shafted instruments of Intuitive Surgical’s da Vinci robot is the tip-mounted wrist. While the standard 8-mm-diameter instruments use a wrist comprised of discrete rotary joints, the 5-mm-diameter instruments employ a tendon-actuated snake-like design [see Fig. 1(c)]. With an inserted length of about 50 cm, these instruments have a slenderness ratio of 100 [12].

For cosmetic reasons, it can be preferable in laparoscopic surgery to insert all of the instruments through a single larger incision or port, which is often placed through the umbilicus. These “single-port” systems are comprised of a straight sheath with multiple working channels through which straight-steerable robotic instruments are inserted [see Fig. 2(b)]. These systems can be used for abdominal, gynecological, and urological surgeries and employ straight-steerable arms with a slenderness ratio of about 100 [57]–[64].

Multiarmed endoscopic surgery robots are comparable in design and slenderness ratio to single-port systems and can be tailored to surgery in many different parts of the body. Applications include endoscopic neurosurgery and Natural Orifice Transluminal Endoscopic Surgery (NOTES) procedures that are located relatively near the body orifice, e.g., throat surgery, transurethral bladder, and prostate surgery [31], [65].

3) Low Slenderness Ratios (Steerable Systems): With slenderness ratios of less than about 50, it is possible to make the entire inserted robot length steerable. This approach can be applied, for example, to the straight sheath of a single-port or endoscopic surgery system. This architecture provides greater orientation control of the tip during single-port procedures while also enabling NOTES procedures deeper inside body orifices. Examples include the steerable sheaths of the MedRobotics, Inc. Flex system [see Fig. 2(a)] [30] and Samsung’s NOTES robot [see Fig. 1(d)] [13]. Since the tip-mounted arms need to flex along their proximal length as the sheath is steered, the arms typically employ flexible-steerable designs. Due to limitations of steerable sheath length, these arms have comparable slenderness ratios to those used with straight sheaths.

Cochlear implants use electrode arrays that must be inserted inside the curving lumen of the cochlea. These arrays are about 25-mm long and 0.5-mm diameter yielding a slenderness ratio of 50 [66], [67]. While they are traditionally inserted manually, abrasion with the walls can damage the surrounding nerve cells, and so the development of robotically steerable arrays is an active topic of research. Despite their relatively low slenderness ratio, adding steerability is challenging due to constraints on the cross section. Consequently, robotic attempts to date have been implemented as flexible-steerable systems [68]–[71].

B. Mapping Robot Designs to Clinical Applications

While most of the six design types defined in Section I can be force fit to any clinical application, it is best to select a design type well suited to the application’s slenderness ratio. As a starting point, the prior experience can guide this selection. Table 1 lists example commercial and research robots grouped by design. The six designs and examples are ordered by increasing slenderness ratio. Sections II-B1–II-B6 below detail the suitability of each design for applications requiring steerable, straight-steerable, and flexible-steerable robot implementations with the preferred implementations listed in the headings.

1) Soft Robot Designs (Flexible-Steerable): The field of soft robotics is undergoing rapid development, and it is not clear at this time what its limitations will be and what advantages it will provide over other designs. While soft robot implementations to date have been low-slenderness-ratio steerable systems, the earliest work demonstrated

Table 1 Comparison of Continuum Robot Design Properties. The Type Column Refers to the Cases Illustrated in Fig. 2. The Medrobotics, Inc. Flex System Is Not Circular, so Cross Section Width and Height Are Given for Diameter. For Robots With Two Telescoping Segments, Two Diameters (Proximal and Distal) Are Given. The Slenderness Ratio Is Computed Using Diameter of Proximal Segment

Design Type	Continuum Robot System [reference]	Type	Length [mm]	Diameter [mm]	Slenderness Ratio, L/d
Soft	STIFF-FLOP Modular Surgical Manipulator [18]	Steerable	100	32	3
	Micro-hydraulic catheters [17]	Steerable	80	3	27
Tendon-actuated discrete-jointed	Medrobotics Flex Robotics Probe [72]	Steerable	170	18 × 28	9
	I^2 Snake Robot [73]	Steerable	366	16	23
	Highly Articulated Robotic Probe (HARP) [29], [74]	Steerable	300	12	25
	Intuitive surgical 5 mm diameter endowrist [12]	Straight-Steerable	500	5	100
Multi backbone	SJTU Single Port Robot [60], [61]	Straight-Steerable	145	6.3	23
	Titan Medical Enos Single Port Robot [57], [76]	Straight-Steerable	300	8	38
	IREP Single Port Robot [58], [77]	Straight-Steerable	450	6.4	70
	Trans-urethral [64] and Transoral airway [78]	Flexible-Steerable	850	5.0, 1.6	170
	Transoral airway [79]	Straight-Steerable	900	4.2	214
Concentric tube	Bimanual Endoscopic Robot [80]	Straight-Steerable	140	1.7	82
	Transnasal Surgery Robot [81]	Straight-Steerable	259	2.3	113
	Robotic Intracardiac Catheter [82]	Straight-Steerable	670	3.7	180
Tendon-actuated	Auris Monarch Robotic Bronchoscope [83], [84]	Flexible-Steerable	~ 600	5.9, 4.2	102
	Intuitive Surgical Ion Robotic Bronchoscope [50], [83]	Flexible-Steerable	~ 600	3.5	171
	Hansen Medical Sensei Robotic Catheter [92]	Flexible-Steerable	830	4.5	184
Magnetically-actuated	Aeon Scientific Robotic Catheter System [86]	Flexible-Steerable	700	4	175
	Robotic Colonoscope [87], [88]	Flexible-Steerable	1600	6.5	215
	Stereotaxis Robotic Catheter System [37], [89]	Flexible-Steerable	~ 1000	2.3	435
	Magnetecs Robotic Catheter System [38], [90]	Flexible-Steerable	~ 1000	2.3	435

that they can be fabricated as catheters with diameters on the order of several millimeters [16], [17], which is appropriate for flexible-steerable devices. The widespread use of balloon catheters, which provide radial expansion, a degree of freedom unachievable by other designs, suggests that soft robots may offer advantages at high slenderness ratios.

2) Tendon-Actuated Discrete-Jointed Designs (Steerable and Straight-Steerable): Serial connections of discrete joints have been employed to create steerable sheaths for endoscopic and NOTES robots. These include MedRobotics steerable endoscopic sheath [29], [91] and the steerable sheath of Samsung's NOTES robot [13]. This architecture has also been used in Intuitive Surgical's 5-mm straight-steerable laparoscopic instruments. This architecture can be used to achieve high flexural stiffness for diameters of about 5 mm or larger.

3) Multibackbone Designs (Straight-Steerable): These designs represent an alternative approach to increasing robot bending stiffness from what can be achieved with tendon actuation while maintaining a continuum design. Here, the push–pull backbones contribute to the overall flexural stiffness of the robot. Furthermore, the ability to concentrically place tubular backbones allows serial stacking of continuum segments without a significant increase in the lost cross-sectional area for delivering actuation. While this architecture has been used in both straight-steerable and flexible-steerable designs, limited mass-manufacturing processes for these robots increase their cost relative to tendon-actuated robots and so make them best suited to straight-steerable implementations that require enhanced stiffness.

4) Concentric Tube Designs (Straight-Steerable): This architecture represents an alternative approach to providing high bending stiffnesses at robot diameters of about 1–3 mm. A shortcoming of this architecture is that it exhibits instabilities due to an interplay between torsional and flexural deformation. Since avoiding these instabilities places limits on the steerable length, these robots are most often implemented as straight-steerable designs with straight sections of high torsional stiffness [81], [82]. While tendon-actuated designs are capable of smaller radii of curvature and larger steering angles, concentric tube designs provide higher flexural stiffness. This quality makes them well suited for use as the bimanual tip-mounted arms of endoscopic single-port robots [80].

5) Tendon-Actuated Designs (Flexible-Steerable): This technique is the most common steering method. The most significant advantages of tendon actuation are the small radii of curvature and large bending angles that it can achieve. While it can be used for all slenderness ratios, its use is most prevalent in robotic versions of high-slenderness-ratio manual instruments. For example, Hansen Medical's electrophysiology catheter was tendon actuated [92], [93]. The intellectual property used in these catheters has been more recently applied to Auris Health's Monarch endoscopic robot (J&J) [28], [83]. Intuitive Surgical has introduced a similar platform, the Ion, for bronchoscopic biopsy [83], [94], [95].

6) Magnetically Actuated Designs (Flexible-Steerable): Magnetic actuation offers the advantage of applying torques and forces directly to the robot (usually the tip) rather than relying on transmission through the body of the robot, which is subject to friction and hysteresis. These torques and forces are relatively small, however, since they are proportional to the amount of ferromagnetic material incorporated in the robot. For applications, such as flexible-steerable electrophysiology catheters, for which small catheter tip forces are desirable, magnetic actuation is well-suited [37]–[39]. In a colonoscopy, where the tortuous curves and elasticity of the colon make insertion and steering difficult, magnetic pulling of the tip is also being investigated [87].

C. Design Procedure

Medical continuum robot designs are driven by application requirements and assessed by various measures of performance. These include size and structure constraints (diameter and length, continuity, and inner lumens), kinematic properties (workspace, curvature, degrees of freedom, and dexterity), and strength properties (output stiffness, load capacity, and elastic stability). In addition, it is often important to consider methods of accessing the surgical site and actuating the robot through a potentially long and tortuous insertion pathway (actuation transmission efficiency, follow-the-leader insertion, and endoscopic deployment). All these inform the choice of continuum architecture and further design choices within the architecture.

1) Structure and Force: The first step in the design process is to determine the type of robot structure based on the clinical application, i.e., whether steerable, straight-steerable, or flexible-steerable is needed, as illustrated in Fig. 2. The clinical application will also constrain the maximum robot diameter and the required length, leading to a certain slenderness ratio, as illustrated in Fig. 3. Table 1 provides the diameter and length for several examples of each system type. Next, the designer should determine the therapeutic tools that the robot must deliver, their sizes, and the approximate range of force that the robot needs to be capable of to guide the tools and perform any clinical tasks. To do this, the medical literature can be consulted, or the forces can be measured experimentally by instrumenting existing tools in collaboration with clinicians [96].

While the force capacity of conventional rigid-link robots is determined by the arrangement of links and the torque capacity of the motors, continuum robot force capacity is primarily influenced and limited by the deformation of the material. That is, while the continuum robot is able to increase the force on an object by actuation, this will entail some structural deformation, and there is a practical limit to the force due to, e.g., strain limits, actuation limits, buckling, or deflections exceeding the anatomical bounds. A useful performance metric in this regard is *output stiffness*, which is the force/displacement relationship felt at the tip of the manipulator when the actuators are held in fixed positions. Force capacity generally increases with output stiffness, but it also depends on the range of motion the robot can achieve through actuation in the direction of the desired force since a force causing deflection must be compensated by actuation. Concentric tube robots have the largest output stiffness for their diameter because they are composed of solid metal tubes. However, their actuatable range of motion is often lower due to curvature limitations. Multibackbone and tendon-driven robots have lower stiffness but a higher actuatable range of motion. In the design phase, force capacity for a chosen architecture can be predicted using kinetostatic modeling, as discussed in Section III.

2) Kinematic Design: The required kinematic design should be determined by the anatomical constraints and task motion requirements. This involves first determining the *workspace* of positions that the robot is required to reach and the *dexterity* required to perform the tasks. These requirements are then mapped onto kinematic requirements for the robot's basic structure to determine the broad kinematic aspects of the design. A helpful abstraction is to visualize the robot as a set of "bending segments" concatenated in series, which are each somewhat independently controllable. The workspace associated with this geometry is then generally trumpet-like, emerging from a single point at the base, with the outer boundary largely determined by the minimum radius of curvature that the segments can achieve. Dexterity refers to the range of end-effector orientations that are possible at a given reachable point. High dexterity is necessary for a continuum robot to perform certain surgical tasks, such as grasping tissue from the desired angle and suturing. The kinematic design challenge is to use workspace and dexterity requirements to synthesize how many actuatable sections the robot will have, what motion each section will be capable of (bending in one or two directions, telescoping, and twisting), and a minimum radius of curvature for the segments.

The radius of curvature of a continuum robot segment is usually limited by material strain. For a solid tube or backbone rod component of a continuum robot, the minimum radius of curvature is

$$\rho_{\min} = \frac{D_o}{2\epsilon_{\max}} \tag{1}$$

where D_o is the outer diameter and $\epsilon_{\max}$ is the design strain limit. Superelastic NiTi is the most common structural material for medical continuum robots. Its strain plateau occurs around 3% (although it can withstand cyclic loading up to 5% with minimal cycle-dependent degradation of its properties).

Based on the results of these analyses, a specific continuum architecture can be selected using Table 1, and a final design can be optimized for the application. In general, kinematics, structure, and force capacity are all coupled, and the designer may need to iteratively evaluate them all several times before converging to a particular architecture and design.

There may often be several potential kinematic designs that are sufficient to meet the task requirements but contain tradeoffs in terms of size, stiffness, and kinematic properties. At this stage, many researchers have

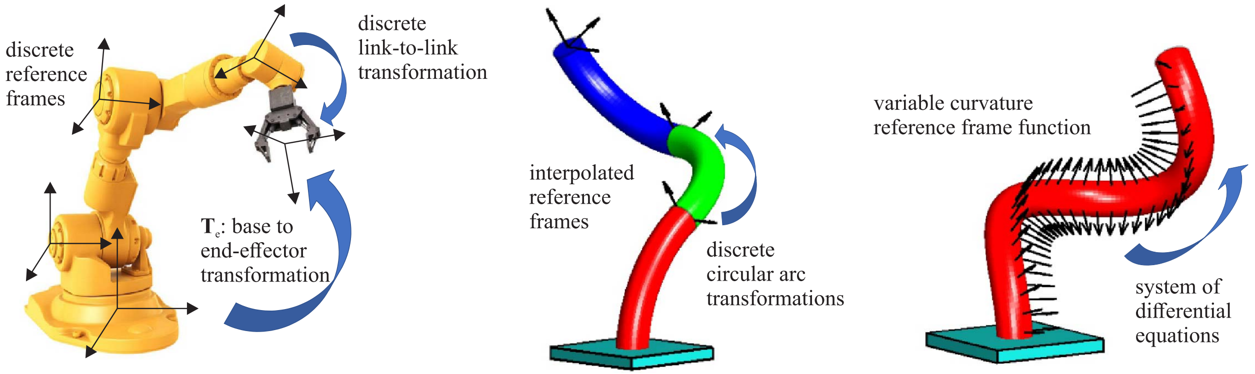

(a) Rigid-Link Robot (b) Simplified Model: Piecewise-Constant Curvature (c) Variable Curvature Model

Fig. 4. ***Continuum robot kinematics models differ from conventional rigid-link models in which they must capture bending along the entire length, rather than at discrete joints only. (a) Rigid link robot with kinematics computed using coordinate frames attached to each robot link. The end-effector coordinate frame is related to base coordinate frame by transformation, $T_e(q)$. (b) Simplified continuum robot models use the geometric assumption that robot shape consists of piecewise-constant curvature circular arcs. (c) More general continuum robot models account for variable curvature deformations, material mechanics, and external loads. The shape is the solution to a set of differential equations.***

employed model-based design optimization. For example, algorithmic design of concentric-tube robots has sought to minimize robot length and curvature while ensuring stability [5], enhance triangulation for dual-arm cooperation [97], or achieve follow-the-leader deployment [98]. Many design optimization efforts have leveraged techniques from the field of computational motion planning. The design of actuation wire paths within a steerable soft robot body was solved by simultaneous path-planning and mechanics simulation [69].

Given a design obtained by the process and considerations above, a robot can be fabricated using standard medical device manufacturing techniques (e.g., micromachining, pulsed laser machining, various methods for heat treatment of nickel–titanium tubes, braided catheter construction methods, and polymer molding methods). The next step is to develop modeling and control algorithms, as described in Sections III and IV.

III. CONTINUUM ROBOT MODELING

Mathematical models of continuum robot behavior have been a critical part of the design, planning, control, and sensing in many surgical applications. The first and most basic models were purely kinematic (dealing only with robot shape and quasi-static motion), but models additionally dealing with material behavior (mechanics models), external forces (kinetostatic models), and inertial effects (dynamic models) have now been incorporated into design and control due to their ability to predict useful aspects of performance, such as output stiffness. These modeling efforts are often analogous to established model formulations for conventional rigid-link robot models but with some important differences due to their continuous and flexible structure.

A. Rigid-Link Robot Kinematics

As shown in Fig. 4 (left), conventional kinematics models for rigid-link robots use a homogeneous transformation matrix to represent the position and orientation (collectively called the "pose") of each link in space. Thus, the matrix

$$\mathbf{T}_i = \begin{bmatrix} \mathbf{R}_i & \mathbf{p}_i \\ 0\;0\;0 & 1 \end{bmatrix} \in \mathrm{SE}(3)$$

represents the pose of link i with respect to some global coordinate system, where $\mathbf{R}_i \in \mathrm{SO}(3)$ is the rotation matrix, and $\mathbf{p} \in \mathbb{R}^3$ is the position vector of a reference point on the link. $\mathbf{T}_i$ can be thought of as a Cartesian coordinate system attached to link i and moving with it, as depicted by the black arrows in Fig. 4. Now, ${}^{i-1}\mathbf{T}_i(q_i) \in \mathrm{SE}(3)$ represents the transformation from link $i-1$ to link i, as

$$\mathbf{T}_i = \mathbf{T}_{i-1}{}^{i-1}\mathbf{T}_i(q_i) \tag{2}$$

and is a known function of the joint actuation variable q_i and other geometric constants (often written using the Denavit–Hartenberg convention [99], but see [100] for a discussion of methods based on screw-theory). The forward kinematics model for the manipulator then computes the end-effector pose $\mathbf{T}_e$ as a function of the joint variables $\mathbf{q} = [q_1\ q_2\ q_3, \ldots,\ q_n]^\top$ by recursively applying (2) from the beginning to the end of the serial chain.

B. Continuum Robot Kinematics

In contrast to rigid-link robots where all deformation is lumped into discrete joints, continuum robots change their shape continuously along the length. This is analogous to a rigid-link robot with an infinite number of joints and infinitesimally small links. In order to represent this smooth shape change with a finite set of parameters, early continuum robotics researchers established a kinematic representation consisting of multiple circular arc segments connected in series, as shown in Fig. 4 (middle). This idea is usually referred to as a *piecewise-constant curvature*

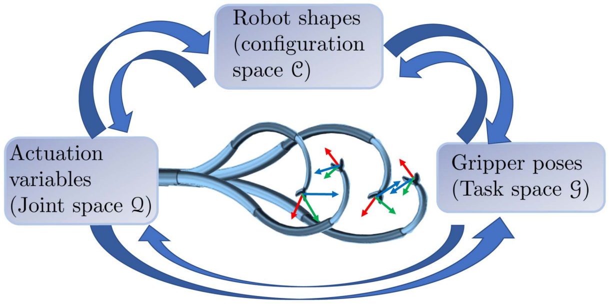

Fig. 5. ***Kinematic mappings used for control and modeling.***

model because the curvature in each segment does not vary over its length. In a piecewise-constant curvature model, the forward kinematics can be written recursively using a constant-curvature transformation ${}^{i-1}\mathbf{T}_{cc,i}(\boldsymbol{\psi}_i)$ that expresses the pose of a segment with respect to the previous segment

$$\mathbf{T}_i = \mathbf{T}_{i-1}{}^{i-1}\mathbf{T}_{cc,i}(\boldsymbol{\psi}_i) \tag{3}$$

where $\boldsymbol{\psi}_i$ is a vector of configuration variables that define the geometry of the constant curvature segment. As reviewed in [101], most constant-curvature models have used so-called "arc parameters" (curvature κ, angle of the bending plane ϕ, and arc length ℓ) as the configuration variables, but other possible choices include azimuth and elevation angles [31], or Cartesian curvature components, κ_x and κ_y, which have the advantage of avoiding a parametric singularity when the segment is straight [33], [102]–[105]. Written in terms of Cartesian curvature components, the constant-curvature transformation matrix can be succinctly expressed as the exponential of the 4 × 4 twist matrix $\hat{\boldsymbol{\xi}}$ multiplied by the length ℓ as follows:

$$\mathbf{T}_{cc} = e^{\hat{\boldsymbol{\xi}}\ell} \quad \text{where} \quad \hat{\boldsymbol{\xi}} = \begin{bmatrix} 0 & 0 & u_y & 0 \\ 0 & 0 & -u_x & 0 \\ -u_y & u_x & 0 & 1 \\ 0 & 0 & 0 & 0 \end{bmatrix} \tag{4}$$

which has a closed-form solution, as shown in [33] and [103]–[106]. While the sequence of constant curvature transformations yields the pose at the end of every segment, the continuum of poses between segment ends can be easily calculated by applying (4) at interpolated arc lengths between 0 and ℓ. The constant curvature framework can also be generalized to include constant torsion, shear, and extension [106].

The configuration $\boldsymbol{\psi}_i$ of each link is a function of some subset of the robot actuation variables, which could include, e.g., translations of tendons or secondary backbones, rotations and translations of precurved tubes, or fluid pressures or volumes. Fig. 5 depicts this idea in the abstract. Regardless of the continuum robot design, there are mappings that relate the following three spaces.

1) *Joint Space* $(\mathcal{Q} \subseteq \mathbb{R}^{n_q})$*:* The set of all possible actuator values within the design constraints of the robot.
2) *Configuration Space:* The set of all possible attainable shapes $(\mathcal{C} \subseteq \mathbb{R}^{n_c})$.
3) *Task Space* $[\mathcal{T} \subseteq SE(3)]$*:* The set of reachable end-effector poses (positions and orientations)

where n_q is the number of actuation variables and n_c is the number of configuration parameters. These three spaces are parameterized by their corresponding joint space vector of actuator positions $\mathbf{q} = [q_1 \quad q_2, \ldots,]^\top \in \mathcal{Q}$, the configuration vector $\boldsymbol{\psi} = [\boldsymbol{\psi}_1^\top \quad \boldsymbol{\psi}_2^\top, \ldots,]^\top \in \mathcal{C}$, and the end-effector pose $\mathbf{T}_e \in \mathcal{T}$.

For motion planning and control in a constant-curvature framework, the inverse kinematics problem must be solved. That is, for a given pose in the task space, what actuator values $\boldsymbol{q}$ are necessary? This problem has been approached by solving two subproblems related to the intermediate configuration space, as shown in Fig. 5. The first problem is known as the *task-to-configuration inverse kinematics* (TCIK: $\mathbf{T}_e \rightarrow \breve{\boldsymbol{\psi}}$) that finds a configuration $\breve{\boldsymbol{\psi}}$ for a desired end-effector pose $\mathbf{T}_e \in SE(3)$. The second problem is the *configuration-to-joint space inverse kinematics* (CJIK: $\breve{\boldsymbol{\psi}} \rightarrow \breve{\boldsymbol{q}}$) that finds the necessary actuation variables $\breve{\boldsymbol{q}}$ for a given configuration $\breve{\boldsymbol{\psi}}$. The TCIK problem can have many solutions for the desired end-effector pose since the segments are chained serially. In contrast, the CJIK usually has a single solution for most continuum robots. The inverse kinematics of a three-segment continuum robot was solved in closed-form in [107]. The inverse kinematics for a general n-segment continuum robot was solved numerically in [108] using the robot Jacobian and integrating the configuration space rates to converge to the desired end-effector pose.

A more general modeling approach for continuum robot kinematics is to represent the kinematic transformations in a differential form that allows variable curvature and shape change along the length. As depicted in Fig. 4 (right), instead of a finite series of matrix multiplications of the segment-to-segment transformations, one can write a differential equation describing how the transformation matrix continuously evolves with respect to s, the reference length along the robot

$$\frac{d\mathbf{T}}{ds} = \mathbf{T}\widehat{\boldsymbol{\xi}} \quad \text{where} \quad \widehat{\boldsymbol{\xi}} = \begin{bmatrix} 0 & -u_z & u_y & v_x \\ u_z & 0 & -u_x & v_y \\ -u_y & u_x & 0 & v_z \\ 0 & 0 & 0 & 0 \end{bmatrix} \tag{5}$$

where the components of $\widehat{\boldsymbol{\xi}}$ describe bending curvature (u_x and u_y), torsion (u_z), shear (v_x and v_y), and elongation (v_z). If these quantities are general functions of s, the pose $\mathbf{T}$ can be numerically integrated as an initial value problem from the base of the continuum robot to the tip. Because of its generality, this type of variable

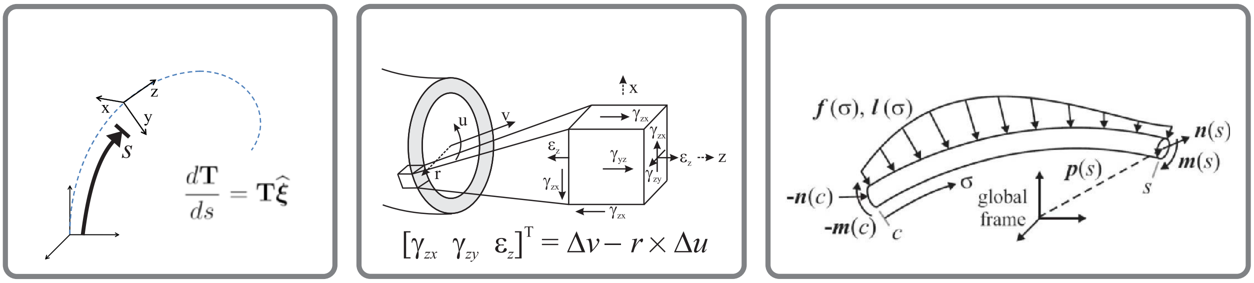

(a) Kinematics (b) Material Mechanics (c) Equilibrium

Fig. 6. ***Continuum robot models are built around three main components. (a) Kinematics relate curvature to the position and orientation along with the robot. (b) Constitutive material laws relate stress to strain, linking internal forces to kinematics. (c) Equilibrium equations balance the internal and external loads on the robot. Continuum robot modeling efforts can be categorized based on the choices made in each of these parts.***

curvature framework (e.g., [109] and some other references) is often used in models for external loading and to describe concentric tube robots whose design is not easily described by a constant-curvature framework due to mechanical complexities that cause variable rates of torsion and bending.

C. Continuum Mechanics and Equilibrium

While the configuration of a traditional rigid-link robot is a function of only the joint variables, continuum robots present a modeling challenge because the configuration can also depend on external loading and material properties. To address this challenge, classical models of slender elastic objects, such as Cosserat rod theory, have emerged as powerful tools for predicting robot deformation in response to internal actuation and external loads. As illustrated in Fig. 6(c), the equilibrium equations of a Cosserat rod relate the internal force $\mathbf{n} \in \mathbb{R}^3$ and internal moment $\mathbf{m} \in \mathbb{R}^3$ carried by the rod in response to external distributed forces $\mathbf{f} \in \mathbb{R}^3$ and moments $\mathbf{l} \in \mathbb{R}^3$ along it as

$$\begin{aligned}\frac{d\mathbf{n}}{ds} + \mathbf{u} \times \mathbf{n} + \mathbf{f} &= \mathbf{0}\\ \frac{d\mathbf{m}}{ds} + \mathbf{u} \times \mathbf{m} + \mathbf{v} \times \mathbf{n} + \mathbf{l} &= \mathbf{0}\end{aligned} \tag{6}$$

where all quantities are expressed in the body-frame $\mathbf{T}(s)$ axes. As shown in Fig. 6(b), the material strain at a point in the rod cross section is related to the kinematic variables in $\boldsymbol{\xi}$ from (5). Thus, the material properties and the geometry of its cross section determine how the internal loads produce the robot shape. While nonlinear material models may be used, many continuum robot modeling efforts have adopted the conventional linear stress–strain relationship, which leads to a linear constitutive law

$$\begin{bmatrix}\mathbf{n}\\ \mathbf{m}\end{bmatrix} = \mathbf{K}\begin{bmatrix}\mathbf{v} - \mathbf{v}^*\\ \mathbf{u} - \mathbf{u}^*\end{bmatrix} \tag{7}$$

where $\mathbf{K} = \mathrm{diag}(AG, AG, AE, EI_x, EI_y, GI_z)$, A is the cross section area, E is Young's modulus, G is the shear modulus, and I_x, I_y, and I_z are the second area moments of the cross section. The variables $\mathbf{v}^*$ and $\mathbf{u}^*$ are vectors corresponding to the stress-free shape of the rod through (5). The complete description of a single rod can be obtained by solving the system of differential equations (5)–(7) subject to suitable boundary conditions. While a complex continuum robot is often not well-described by a single rod model, rod-like structures are often used as components of continuum robots (e.g., concentric precurved tubes, primary backbones, secondary backbones, catheter tubes, and guidewires). As such, Cosserat rod equations have been instrumental in the derivation of several fundamental models for continuum robots (e.g., [3], [111], and [112]), describing their general large-deflection response to external loads and actuation forces.

D. Architecture-Specific Modeling

The different continuum robot architectures discussed in Section I each entail various modeling requirements and challenges. As such, while continuum robot models are generally based on the common frameworks described above, architecture-specific mathematical models have mostly been developed in an *ad hoc* way to meet the needs of their unique features and requirements.

1) Tendon-Actuated Models: Tendon-actuated continuum robots rely on the transmission of forces to a central backbone or substrate structure by means of cables (tendons) in order to change the shape. Early models were purely geometric [111] and based on constant-curvature, as reviewed in [101]. Constant curvature beam mechanics models for tendon-actuated robotic catheters, including tendon stretch and segment coupling, were developed in [26] and [27], and an analytical model for controlling tendon tension was developed by Dalvand *et al.* [112]. Tendon-actuated robots offer some flexibility in design since the tendon routing paths can be chosen as curves in space. These general paths and external loads were modeled in [112] and [116] with a 3-D Cosserat rod approach. A confounding issue in tendon-robot modeling is loss of tension loss due to static friction. This was modeled using the Dahl friction in [114], and Liu and Alambeigi [115] analyze how frictional losses are coupled with external loading. Various numerical modeling approaches for tendon-actuated robots are reviewed in [116].

2) Discrete-Link Models: Discrete-link tendon-actuated robots are modeled in the conventional rigid-link kinematics paradigm, but these structures are typically underactuated (fewer actuators than kinematic degrees of freedom), requiring some additional criteria to resolve the redundancy and determine the shape. Often, the redundancy is resolved by considering the elasticity of the structure and performing energy minimization subject to the actuation constraints. For the surgical snake robot design known as the highly articulated robotic probe (HARP) developed by Choset's group, redundancy is resolved by accounting for actuation history since the robot is designed for a specific gait cycle that deploys it in a follow the leader fashion [117].

3) Multibackbone Models: Multibackbone robots use multiple beams (often tubular) in push–pull actuation to achieve their equilibrium shapes. They have a parallel kinematic architecture since the end disk of a multibackbone robot, as shown in Fig. 1, is supported by a central (primary) backbone and a collection of actuated (secondary) backbones. Early models of multibackbone robots assumed piecewise-constant curvature (e.g., [31]) and experimental investigations showed that these assumptions hold well for robots ranging from 1.6- to 10-mm ODs with lengths of segments ranging from 20 to 140 mm [118], [119].

Under a constant-curvature framework, the static equilibrium of multibackbone robots can be formulated by conservation of power argument, as in [120]. Validation against experimental data and more accurate models in [121] showed high accuracy, and a close-to-circular bending shape can be ensured by careful design of the spacing between the spacer disks. Modeling multibackbone robots is still an active area of research due to the tradeoffs of generality (relaxing assumptions around torsion, friction, out-of-plane bending, and routing path as in [122]) and increasing computational speed as in [123].

4) Concentric Tube Models: A unique challenge of concentric tube robots is the presence of significant torsional deformation in the tubes during normal robot operation in free space, which affects accuracy in modeling, design, planning, and control. Early models of concentric tube robot mechanics were quickly generalized to include the effect of torsion [3], [4], [124], [125] by using energy methods and the Cosserat rod theory. The interaction of bending and torsion along the robot produces a resultant shape that does not fit the piecewise constant curvature paradigm. As a result, the shape of the robot is no longer a closed-form expression and instead must be obtained by a numerical integration along the length. Furthermore, models describing how external loading affects concentric tube robot shape employed Cosserat rod theory to describe each tube in the robot [35], [36], and tube dynamics were similarly modeled in [126].

As discussed above, certain concentric tube designs can exhibit a "snapping" elastic instability when two curved concentric tubes are rotated, in which the robot rapidly transitions to a new equilibrium state [124]–[126]. Methods for determining the stability of a given model solution have been developed using calculus of variations [127] and the optimal control theory [128] to predict general stability under external loads. These stability models have been useful for developing planners and controllers that can avoid physical instabilities [129]–[135] and reduce the possible instability by optimizing the robot design [127], [136]–[140].

The existence of intertube clearance and friction is also a practical issue that can affect modeling accuracy. Relaxing these assumptions has so far been challenging to do without drastically increasing the complexity of the model frameworks. However, some progress has been made by lumped friction models [141] and computationally efficient contact models [142], [143].

5) Magnetically Actuated Models: Magnetically actuated catheters and continuum robots can be simply modeled as a single rod acted on by external forces. However, additional complexity arises in the model for the magnetic field that generates forces and torques on magnetized portions of the catheter [144]. Early modeling work for position control was done by Tunay [40], [41] at Stereotaxis Inc. and later expanded in [42] based on a quaternion representation of Cosserat rods. Liu *et al.* [11] developed a model for MRI steered robotic catheter in a constant-curvature framework. Edelman *et al.* [44] developed a Cosserat rod framework and calculated the necessary Jacobians for catheters with permanent magnetic components subject to spatially varying magnetic fields. Kratchman *et al.* [145] used a Kirchhoff rod model for control, steering the catheter using an external permanent magnet manipulated by a robot. Peyron *et al.* [146] have used continuation methods to analyze solution bifurcations in the solution landscape.

6) Soft Robot Models: Significant early work on mechanics models of soft robots was done by Trivedi *et al.* [147] using the Cosserat rod theory to describe the OctArm, a large-scale soft robot actuated by pneumatic McKibben muscles. The main modeling challenge unique to such fluid-driven soft robots has been understanding the coupled relationship between actuation pressures/volumes and robot deformation. While models based on the rod theory [106] or even constant curvature [148] can be adequate for slender robot designs, some soft robot designs exhibit modes of deformation not captured by these conventional methods, such as cross section deformation associated with inflation (modeled in [42]) and the unfolding of convoluted bellows-type structures [149], which is usually tackled by full nonlinear finite element analysis in 3-D.

This gains accuracy but increases the computational cost versus a simpler model, usually making the model unsuitable for real-time control and planning. However, recent efforts toward real-time FEM via order reduction [150] and coupling detailed models to simpler ones [151] have somewhat bridged this gap.

E. Differential Kinematics and Statics

Any of the kinematic and static models discussed above can be linearized at a given robot configuration to provide the relationship between small changes in the actuator displacements $\mathbf{q} \in \mathbb{R}^{n_q}$, actuator forces $\boldsymbol{\tau} \in \mathbb{R}^{n_q}$, end-effector pose $\mathbf{T}_e \in \mathrm{SE}(3)$, and end-effector wrench $\mathbf{w}_e \in \mathbb{R}^6$ (force and moment). For any continuum robot, the linearized relationships between these quantities can be written in the following form [152]:

$$\begin{aligned} \boldsymbol{\xi} &\equiv \left(\mathbf{T}_e^{-1}\dot{\mathbf{T}}_e\right)^{\vee} = \mathbf{J}\dot{\mathbf{q}} + \mathbf{C}\dot{\mathbf{w}}_e \\ \dot{\boldsymbol{\tau}} &= \mathbf{K}\dot{\mathbf{q}} + \mathbf{W}\dot{\mathbf{w}}_e \end{aligned} \tag{8}$$

where $\dot{\ }$ denotes a derivative with respect to time, $\vee$ maps $\mathfrak{se}(3)$ to $\mathbb{R}^6$ [153], $\mathbf{J}$ is the body-frame manipulator Jacobian, $\mathbf{C}$ is the compliance matrix, and matrices $\mathbf{K}$ (input stiffness) and $\mathbf{W}$ (reflectivity) describe how the actuator forces are affected by changes in $\mathbf{q}$ and $\mathbf{w}_e$. Note that a rigid-link robot is considerably simpler because $\mathbf{C} = \mathbf{0}$, $\mathbf{K} = \mathbf{0}$, and $\mathbf{W} = \mathbf{J}^{\top}$.

In a general variable-curvature robot model expressed as a set of differential equations (e.g., models built on the Cosserat rod theory), these matrices can either be approximated by finite differences on the numerical model solution [154] or by integrating the derivative of the original model differential equations with respect to the variables involved [152], [155].

Equation (8) implicitly accounts for the elastic energy of the robot. For a general bending shape, this would require the full solution of the mechanics equations. If, however, a continuum robot is designed to bend in known shapes (e.g., circular bending subject to small loads), then one may express the elastic energy E of the robot as a function of its configuration. In this case, one can write a power balance stating that the net power input from actuation and external loading is equal to the rate of change of elastic energy stored in the device

$$\dot{\mathbf{q}}^{\top}\boldsymbol{\tau} + \boldsymbol{\xi}^{\top}\mathbf{w}_e = \dot{E} \tag{9}$$

where E is the total elastic energy stored in the robot's deformation (gravitational energy is negligible for small surgical robots). For models in the piecewise-constant curvature framework (or some other configuration-space basis parameterized by the vector $\boldsymbol{\psi}$), the differential kinematics can be written as

$$\boldsymbol{\xi} = \mathbf{J}_{\xi\psi}\dot{\boldsymbol{\psi}}. \tag{10}$$

For a desired end-effector twist $\boldsymbol{\xi}$, the configuration speeds[1] $\dot{\boldsymbol{\psi}}$ can be found using the pseudoinverse of $\mathbf{J}_{\xi\psi}$. The corresponding augmented vector of joint speeds may be expressed as

$$\mathbf{J}_{q\psi}\dot{\boldsymbol{\psi}} = \dot{\mathbf{q}}. \tag{11}$$

The conservation statement in energy then requires that the following relation hold [120]:

$$\mathbf{J}_{q\psi_i}^{\mathrm{T}}\boldsymbol{\tau}_i + \mathbf{J}_{\xi\psi_i}^{\mathrm{T}}\mathbf{w}_e = \underset{\psi_i}{\nabla}\mathbf{E} \tag{12}$$

where $\boldsymbol{\tau}_i$ is the joint-level force vector for segment i, $\mathbf{w}_e$ is the vector of wrench (force followed by moment) acting at the end-effector, and $\underset{\psi_i}{\nabla}\mathbf{E}$ is the gradient of the potential energy of the continuum segment.

In the above equations, in forming $\mathbf{J}_{q\psi_i}$ and $\mathbf{J}_{\xi\psi_i}$, one must consider any kinematic coupling between subsequent segments and the transformation of wrench (force and moment) from the end-effector to the frame of the end disk of each segment (e.g., as in [108]).

IV. CONTROL, SENSING, AND PLANNING

Robots are typically controlled by specifying either the desired instantaneous position or velocity of the end-effector. Alternately, to achieve high-speed or precise motions, a trajectory or motion (position versus time) can be specified. While position and velocity control can be achieved using kinematic models and low-cost voltage amplifiers, trajectory control requires a dynamic model of the robot and the use of current amplifiers to achieve the necessary motor torques for trajectory control.

While the kinematic and dynamic model parameters of rigid robots can be easily measured, this is not the case with continuum robots. Furthermore, continuum models also include constitutive and elastic parameters, which are equally difficult to estimate. In addition, while rigid robots typically operate so that only their end-effector is in contact with the environment, continuum medical robots often experience contact along the entire length inserted into the body. The associated deflections must be included in the models but are almost never measured.

Since medical robots are small and are required for safety to move slowly, continuum medical robots are often controlled using position control as opposed to motion control. This means that only kinematic and static models are required, thereby avoiding the use of the robot dynamics. While this approach does reduce controller complexity, several key challenges specific to continuum robot control arise as described in the following.

---

[1] We use $\boldsymbol{\tau}$, $\boldsymbol{\psi}$, and $\boldsymbol{q}$ to designate augmented vectors concatenating the respective entities $\boldsymbol{\tau}_i$, $\boldsymbol{\psi}_i$, and $\boldsymbol{q}_i$ for all segments $i = 1, \ldots, N_S$, where N_S is the number of segments.

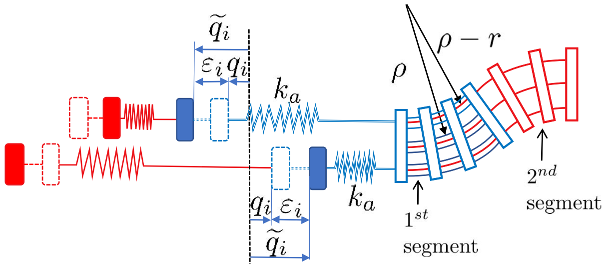

Fig. 7. ***Two-segment multibackbone continuum robot with concentric backbones. The figure depicts the actuation compensation with one backbone under tension and another under compression for the first segment and the opposite for the second segment. Empty dashed-line rounded squares designate the nominal joint-level positions q_i, and the solid-filled ones show the corrected joint positions $\widetilde{q}_i$ with actuation compensation, ε_i. k_a depicts the axial stiffness of the backbones.***

A. Motion and Force Transmission Losses

Continuum robots suffer from motion and force transmission losses. Motion transmission losses arise from extensions/twisting of the actuation transmission lines due to the large forces/torques needed to bend the continuum segments. In multibackbone and tendon-actuated designs, force transmission losses stem from the frictional build-up along the backbone/tendon routing path, which has been shown to resemble the phenomenon of friction build-up in a band brake, i.e., they grow exponentially with the contact angle along the path of the tendon/backbone. In concentric tube robots, motion transmission losses arise from torquing thin-walled tubes in order to overcome distal friction and antagonistic bending moments among the tube pairs.

Regardless of the type of continuum robot used, motion transmission losses can place significant design constraints on the length of transmission lines, their material choice, and the maximal number of continuum segments that can be stacked. These losses corrupt the nominal kinematics model of a continuum robot and cause it to appear unresponsive to the user's commands during telemanipulation.

To illustrate the effect of extension, let us consider a two-segment planar multibackbone robot, as shown in Fig. 7. The robot has the backbones of the distal segment passing through the tubular backbones of the proximal segment. Assuming that the central backbone and the secondary backbones are separated by radial distance r, the nominal actuation stroke q_s associated with bending the proximal segment ±90° is the difference in the arc length between the backbone closest to the center of curvature and the primary backbone

$$q_s = \pm\frac{\pi\rho}{2} \mp \frac{\pi(\rho - r)}{2} = \pm\frac{\pi r}{2} \approx \pm 1.5708\, r. \qquad (13)$$

For $r = 1.5$ mm, the required stroke would be ±2.35 mm. If the backbone actuation lines exhibit motion losses due to backlash and backbone/wire extension of 0.5 mm, this corresponds to a bending angle error of ±19.15°. Experimental validation in [156] on a ∅4.2-mm multibackbone robot using superelastic NiTi backbones (see Fig. 8) for transmission lines ≈900-mm long showed bending errors as high as 53° for a commanded bend angle of 90°.

Since the backbones of the distal segment in Fig. 7 pass through the proximal segment, an error in the actuation of the proximal segment also contributes to an error in the kinematic model of the distal segment. Therefore, using a nominal kinematics model is guaranteed to produce poor open-loop motion tracking. Therefore, actuation compensation is a critical step for enabling precise kinematic models for these robots.

Fig. 8 shows a sample application scenario where coordinated joint-level control with motion compensation is critical for passing circular needles in confined spaces without the need for a distal wrist. By accurately coordinating the joint-level motions, it is possible to use continuum robots to transmit rotation about their backbone. This mode of operation has also been implemented in the da Vinci SP surgical system. The description below explains how such coordinated joint-level motion control and motion compensation can be achieved. Although the example below refers to a multibackbone robot, the challenge of actuation compensation is the same for all continuum robot architectures.

Referring back to Fig. 7, and assuming that each actuation transmission line has a uniform axial stiffness k_a, one may use the vector of predicted backbone forces $\boldsymbol{\tau}$ required to bend the continuum segments at the desired configuration $\boldsymbol{\psi}$ using the statics model of (12). Alternatively, one may directly sense this force by installing load cells in the actuation unit. Given these predicted/sensed forces, one may predict a vector of deflections $\boldsymbol{\varepsilon} = \mathbf{K_a}^{-1}\boldsymbol{\tau}$, where $\mathbf{K}_a$ has the elements k_a along its main diagonal. To compensate for the joint-level control reference signal, one then may apply the predicted deflections in a feedforward fashion such that $\widetilde{\mathbf{q}} = \mathbf{q} + \boldsymbol{\varepsilon}$.

The abovementioned method naïvely applies compensation based on the stiffness model of the robot but

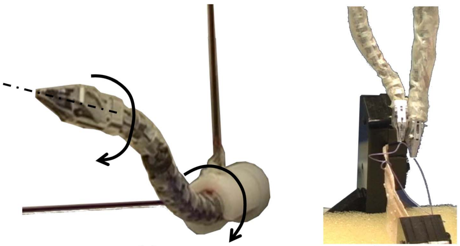
(a) (b)

Fig. 8. ***Rotation transmission along the backbone of a multibackbone robot requires accurate joint-level motion coordination. (a) Rotation about the backbone [79]. (b) Dual-arm suturing where the left arm uses rotation about the backbone, and the right arm is used to for needle hand-off.***

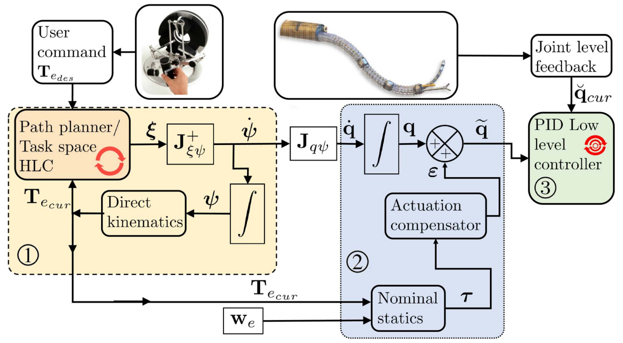

Fig. 9. ***Position control with an HLC for end-effector motion tracking ①, a feedforward actuation compensator ②, and an LLC for joint-level position control ③.***

ignores the effects of friction and material parameter uncertainty. It can significantly improve robot performance but cannot deal with mechanical play (backlash) or with the fact that the statics model in (12) is corrupted with unknown frictional losses. To overcome this challenge, one may wiggle the robot while measuring its motion and comparing it to the commanded signal and then cast the problem as an estimation problem to estimate the backlash parameters and the effect of the axial stiffness parameters (e.g., [156]). Finally, since frictional losses depend on the external load and the geometry of the routing of transmission lines, much more elaborate methods are needed to generalize the actuation compensation approach (e.g., see [157]). One approach requires collecting motion data, estimating hysteresis parameters, and creating several joint-force maps that correspond with the configuration and the configuration speed. Such maps may be encoded in a variety of ways, including support-vector regression. The other approach involves the use of adaptive estimation of the system internal parameters based on elaborate statics and kinematics models. With the successful implementation of actuation compensation, one may achieve motion tracking with very small errors (less than 0.2° per continuum segment).

B. Position Control Using Actuation Compensation or Mixed Source Feedback

Fig. 9 shows the outline of a typical position control loop for continuum robots with actuation compensation. The user's command (e.g., from a telemanipulation device) specifies the desired end-effector frame $\mathbf{T}_{e_{\mathrm{des}}}$, which is then used as an input into a high-level controller (HLC) ①. The HLC ensures end-effector motion tracking via either a path planner/smooth pose interpolation or a resolved rate motion algorithm that calculates at any time the end-effector twist ξ that eliminates the end-effector position and orientation error. Redundancy resolution is then used to solve for the configuration rates for all segments $\dot{\psi}$. The configuration vector of the robot is computed as a time integral of the configuration rates, thereby producing, at any given instant, the reference configuration of all segments ψ. Assuming that the low-level controller (LLC) ③ will use joint-level control to track this reference configuration, one uses ψ as an input to the direct kinematics to calculate the end-effector frame $\mathbf{T}_{e_{\mathrm{cur}}}$ and to provide pose feedback to the task space HLC loop. In making this assumption, we have stipulated that the joint-level controller must run at a significantly higher rate than that of the loop updating the desired pose in order to ensure accurate tracking of the desired configuration.

In Fig. 9, the configuration rates $\dot{\psi}$ are converted to nominal kinematics joint-level speeds $\dot{\mathbf{q}}$ and integrated to provide the desired joint positions $\mathbf{q}$. The pose feedbacks along with the external force and moment $\mathbf{w}_e$ are used as an input to the actuation compensation feedforward compensator ②, thereby producing the corrected joint-reference $\tilde{\mathbf{q}}$. An LLC is used at a higher control rate to close the joint-level error. Usually, this controller has the form of a proportional–derivative–integral (PID) controller.

Since the control framework of Fig. 9 makes use of the statics and stiffness models, and assumes knowledge of the external load, it is not possible to achieve very accurate motion tracking without accurate tuning of stiffness and statics model parameters. One way to overcome this limitation is shown in Fig. 10, where both joint-level and configuration space feedback are used. In addition to the normal joint-level position feedback, this control method requires sensing the configuration variables ψ_{cur} for each segment using magnetic or optical tracking or using integrated fiber-Bragg grating strain sensors within each segment. Instead of using (11) to compute the joint rates, one may use a mixed (configuration and joint space) feedback in the form

$$\dot{\mathbf{q}} = \mathbf{C}\,\mathbf{J}_{q\psi}\,\dot{\psi} + \mathbf{K}_{\psi}\mathbf{e}_{\psi} \tag{14}$$

where $\mathbf{C}$ is a diagonal gain matrix containing the model-based compensation factors that can be precalibrated for each segment in an unloaded configuration to achieve minimal error between the commanded ψ_i and the

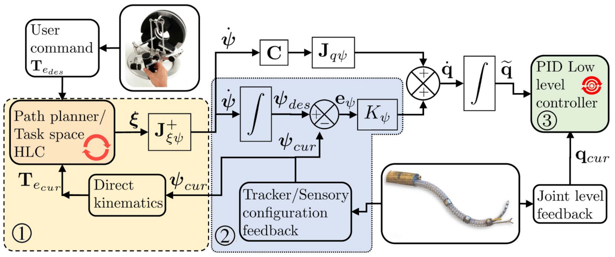

Fig. 10. ***Position control with mixed configuration and joint space feedback, as presented in [158]. Position control with an HLC for end-effector motion tracking ①, a proportional gain configuration space rectifier ②, and an LLC ③ for joint-level position control.***

actual ψ_i [156]. The first term $\mathbf{C}\mathbf{J}_{q\psi}\,\dot{\psi}$, therefore, designates the configuration-to-joint space kinematics corrected by a model-based compensator $\mathbf{C}$. The second term $\mathbf{K}_{\psi}\mathbf{e}_{\psi}$ is a proportional feedback with a diagonal positive definite gain matrix $\mathbf{K}_{\psi}$. The configuration space error is defined as $\mathbf{e}_{\psi} = \psi_{\text{des}} - \psi_{\text{cur}}$.

This mixed feedback approach has been shown by Bajo *et al.* [158] to significantly reduce pose tracking errors and help overcome moment coupling effects between adjacent segments. This approach has also been recently adapted in [166] and [167] for a continuum robot actuated by distal-tip waterjet forces.

In addition to the model-based approaches, Yip and Camarillo [169] presented a sensor-based approach using tracking of the catheter tip to numerically estimate the kinematic Jacobian of the catheter. The method allows for the robustness of control to model uncertainty due to deflections but at the cost of limiting the high-level control frequency to less than the frequency of the tool-tip tracking data. Vrooijink *et al.* [161] have also adapted the model predictive control approach to solve a constrained optimal control problem of steering a catheter using tool-tip feedback via ultrasound imaging.

C. Controlling Contact Forces

Fig. 11 depicts a hybrid direct force/position control framework for continuum robots. This control framework is an adaptation of hybrid force/motion control for rigid-link robots, as presented in [162] and subsequently amended in [163] to account for accurate control task decomposition.

Control task decomposition splits the control task into one task for controlling motion/position in a subspace of allowable twists (motions) and another task for controlling contact forces in an orthogonal subspace of constraint wrenches (forces/moments). The hybrid position/force control task is, therefore, to follow a reference end-effector frame $\mathbf{T}_{e_{\text{ref}}}$ while applying a reference wrench (force and moment) $\mathbf{w}_{\text{ref}}$ on the environment.

A position controller ① computes a desired twist $\boldsymbol{\xi}_{\text{des}}$ that closes the error in end-effector frame, which, in turn, is projected into the subspace of allowable twists using a projection matrix $\boldsymbol{\Omega}_m$ and then converted into a configuration space speed $\dot{\psi}_m$ using the instantaneous inverse kinematics (using $\mathbf{J}_{x\psi}^{+}$).

Similarly, a force controller ② is used to generate an end-effector desired wrench $\mathbf{w}_{\text{des}}$ that closes the error between the current wrench measurement/estimate $\mathbf{w}_{\text{cur}}$ and the reference wrench $\mathbf{w}_{\text{ref}}$. This desired wrench is then projected into the space of constraint wrenches using a projection matrix $\boldsymbol{\Omega}_f$. The resulting wrench is then converted into a generalized configuration space force via $\mathbf{J}_{\xi\psi}^{\mathrm{T}}$ and then turned into a configuration space generalized speed $\dot{\psi}_f$.

The commanded configuration speed $\dot{\psi}$ is then integrated to update the desired configuration ψ, which, in turn, is converted into a reference joint-space command $\mathbf{q}_{\text{ref}}$ while taking into account the actuation compensation ε. Finally, the reference command is used as an input to a low-level joint position controller ③, and the direct kinematics is used to report back the end-effector frame $\mathbf{T}_{e_{\text{cur}}}$.

In the above control framework for direct hybrid force/position control, the control task decomposition requires knowledge of the geometry of contact/constraint in the robot frame. Unlike rigid link robots, the geometry of contact between a continuum robot and the environment is affected by the uncertainty of the direct kinematics and mechanical deflections of the robot. Therefore, Mahvash *et al.* [164] used an indirect force control approach to achieve stiffness interaction control using a concentric tube robot. With an indirect force control approach, the main task remains in position control and the assumption is that one regulates the position to affect a desired deflection/reaction force at the tip of the robot. To achieve this, one needs an approximate stiffness model that can be obtained through a mechanics modeling of the robot and a tip tracking solution (e.g., magnetic tracker coil at the tip of the robot).

Other solutions for force control include the use of dedicated sensors at the robot tip for estimation of tip forces from intrinsic measurements of either robot deflection using FBG sensors or using joint-level load cell measurements. Kesner and Howe [165] used a dedicated miniature load sensor at the tip of a catheter to control one component of interaction force. Bajo and Simaan [166] presented an approach for hybrid force motion control of multibackbone robots using the estimated force at the tip of the robot via a model inversion of the statics model of (12) following the approach of [108]. To achieve force regulation, an estimated configuration space compliance model was used to convert the desired force rectifying signal into a configuration space speed. An improvement over this approach was recently presented in [167] where it was shown that joint-level friction cancellation using support vector regression and use of hybrid admittance/position control allowed useful force regulation while sliding on a surface (force magnitude error of ≈0.2 N).

In addition to force control, compliant motion control is of particular relevance to surgical robots. For example, a continuum robot can conform itself to the unknown geometry of an anatomical passageway by invoking an active compliance control mode. This control mode specifies the configuration speeds $\dot{\psi}$ for each segment based on measurement of joint-level torques τ_i for each segment and based on an inversion of (12) with the condition that the external force at the tip should be minimized (therefore, assumed zero). Successful implementation of this control mode requires accurate cancellation of the internal friction effects of the robot (e.g., using support vector regression as in [168]). Examples of applications of this approach include allowing continuum robots to slide down a nasopharyngeal tube to gain access into the airway [78]. Also, the modelless approach of Yip and

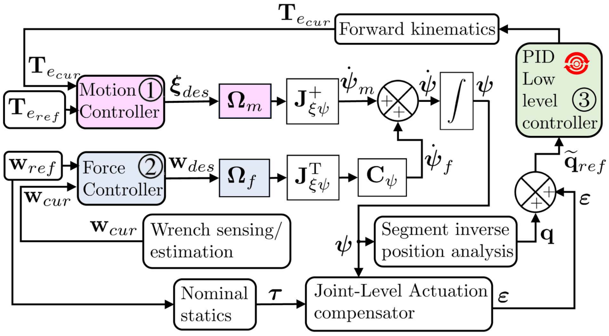

Fig. 11. ***Hybrid motion/force control for continuum robots. A motion controller ① and a force controller ② act in decoupled spaces yielding configuration space speeds that are integrated to produce joint-level reference input to an LLC ③ after implementing actuation compensation.***

Camarillo [169] can also enable force control and active compliance for catheters.

D. Sensing

While it has received limited attention, the application of sensing to continuum robots is very important. Unlike rigid robots, the sensing of continuum robot deformation is crucial for accurate control. Furthermore, providing the clinician with a graphical visualization of the robot shape inside the body can facilitate navigation and improve patient safety. Similarly, the sensing of tip forces and moments is also important both for control and task safety. The small cross section of continuum designs makes the design and integration of shape and tip sensors challenging, however, as described in the following.

1) Shape Sensing: Sensing of curvature and continuum segment shapes has mostly focused on the use of integrated fiber Bragg grating (FBG) sensors within sensory bundles. When a continuum segment bends, an FBG sensor located inside that segment experiences a linear strain, which is detected as a phase shift of the excitation signal. This strain can be interpreted as a measurement of local curvature. By combining such measurements from an array of sensors located along with the robot, the curvature can be integrated to solve for the deflected shape. Lunwei *et al.* [170] demonstrated the potential of this method for shape reconstruction of colonoscopes. Rosenthius *et al.* [171] integrated an FBG array into a tendon-actuated continuum robot and used curvature feedback for control. Subsequently, many works have looked at ways of detecting the shape of continuum robots using FBG sensors.

One particular challenge with FBG sensors is their limited strain tolerance. To overcome this, Liu *et al.* [172] presented a design that allows offsetting an optic fiber from the neutral bending axis of a sensor bundle comprised of two radially and tightly packed nickel–titanium wires and an optic fiber with the FBG pattern. Xu *et al.* [173] explored the use of a helically wrapped FBG along the circumference of a large concentric tube robot. Irrespective of the FBG sensor used, this method of sensing is sensitive to temperature changes and requires the use of an additional FBG sensor for temperature strain-effect compensation.

The optimization of sensor placement for shape reconstruction of a compliant beam has been addressed in [174] to avoid Runge's phenomenon. Also, Kim *et al.* [175] considered the use of modal basis reconstruction with principal component analysis to limit the degree of the basis functions. They used global optimization with a simulation of the robot mechanics to discover the optimal placement of the FBG sensors. Shapiro's results in [174] suggest that one should avoid equidistant sensor placement, and a few sensors are sufficient. Kim's results also suggest that high accuracy may be achieved using a small number of sensors, which also was confirmed in [176] from the perspective of calibration of the bending shape of continuum robots.

2) Contact Detection: Sensing of constrained contact for continuum robots was shown to be possible using monitoring of the joint-level forces or using the deviation of the end-effector motion from the nominal unconstrained kinematics. The motion kinematics can be characterized using joint-level information and configuration space feedback by measuring ψ_i using magnetic tracking coils. While the joint-level force-sensing method is accurate for slow motions, the kinematic method is not due to sensory noise. Therefore, combined use of both of these methods can provide accurate contact detection. These two methods were demonstrated in [177], and the localization of contacts was shown to be within 2–3 mm using magnetic tracking information and a constrained motion kinematics model [178]. Recently, the use of the kinematics-based method has been demonstrated for pneumatically actuated soft robots [179].

3) Force Sensing: Joint-level information can be used to estimate the load on a catheter or continuum robot. In [118], it was shown that inversion of the statics model of (12) can result in accurate force and moment sensing at the tip of a multibackbone robot, and a demonstration of stiffness mapping via mechanical probing of a prostate model was made possible using this intrinsic sensing method. This method has been recently extended in [167] to demonstrate improvement in force regulation based on joint-level sensing using support vector machine regression and hysteresis modeling to account for the impact of friction and motion losses in multibackbone robots. These results showed that joint-based tip wrench sensing (intrinsic force and moment sensing) can be accurate enough to be clinically meaningful for tasks of regulating the tightening of knots or regulating ablation force, even in systems that suffer from large levels of friction force transmission losses.

The inherent compliance of continuum robots also raises the possibility of estimating applied forces based on observations of the deflected robot shape. The use of a kinetostatic model to infer forces based on displacement data was explored for force control of concentric tube robots [164], [180], tendon-actuated robots [181], [182], wire-actuated catheters [183]–[186], parallel continuum robots [152], and other surgical instruments, including loads along the entire instrument length [182], [187]. Finally, deflection-based force estimation models have been approached from a learning perspective [188].

E. Planning

Motion planning generally deals with the problem of coordinating the internal degrees of freedom of a robot to produce purposeful motion in the desired task space. For medical continuum robots, a purposeful motion carries out some part of a medical task while avoiding damage to surrounding tissue. One challenge of motion planning for any hyperredundant robot is that planning occurs in the configuration space, which grows in dimension with the number of degrees of freedom of the system. Much of the research in planning for continuum robots relate to reducing the dimension of configuration space [189]. This reduction is often achieved by only planning for the tip or distal end of the robot and then forcing the rest of the robot to "follow-the-leader" as the distal portion of the robot moves through the space.

The second challenge of continuum robot motion planning is avoiding or minimizing damage to the surrounding tissues through which the robot is moving [189]. Finally, uncertainty with respect to both the robot and its environment, as with many planners, is also a strong consideration when developing planners for continuum robots.

Prior work in motion planning for continuum robots can be categorized based on the type of robot. For example, the HARP snake robot [190] simply aims the tip of the robot, and as it advances forward, the body is forced to follow a curve generated by the tip. This process works well for the HARP because it is a relatively stiff mechanism and it mainly operated in void spaces, not piercing through tissue.

Many motion planning methods for concentric tube robots assume that the planner is given the desired tip path, and the planner performs a series of inverse kinematics operations to direct the robot along the curve [191]. Naturally, the challenge here is computing the inverse kinematics for a high degree of freedom systems. Some early work actually used a simple kinematic model (and intentionally ignored robot/tissue mechanics), in the first place, to determine the path [192], [193]. The rationale for ignoring tissue dynamics and yet using a simplified kinematic model was to enable rapid planning and yet be a good "enough" path that respected the robot/tissue mechanics.

Sample-based planning approaches have been widely used because of their ability to quickly find paths in high-dimensional configuration spaces. The two classic sample-based approaches are probabilistic roadmaps (PRMs) [194] and rapidly exploring random trees (RRTs) [195]. In both approaches, samples are generated by sampling the robot's configuration space—the set of robot configurations (e.g., set of joint values)—and checking if the configuration lies in the free space, i.e., checking to see if the configuration does not intersect an obstacle. The PRM method forms a graph, sometimes called a roadmap, where a node corresponds to a configuration in the free space and an edge connects two nodes if there is a (simple) collision-free path between two nodes. If "enough" nodes are sampled and connected to each other, then a planner uses a PRM to determine a path in the free space by searching for a path between two nodes: one corresponding to the start configuration and the other the goal configuration, in the PRM. The idea here is that these nodes are close to the actual start and goal configurations, thereby finding a path by moving to the PRM, then along the PRM, and then finally to the goal.

The RRT method is similar but is typically a one-time search where the robot forms a tree where the start node is the actual start configuration and iteratively grows the tree until a leaf node is found, which is near the goal configuration. The planner then searches the tree from the root to such a leaf to find a path. The challenge lies in creating the tree. Starting with the start configuration, a configuration is sampled at random from the free space, and if it lies in the free configuration space, the planner searches for a node on the tree that is closest to the sampled configuration. Note that, for the first iteration of this approach, the start node is the tree. The planner then "grows" the tree by determining a sample that is near the closest node on the tree but lies in the direction toward the sampled configuration. An edge is then created between this new node and the closest node, and the process repeats until the tree forms a node near the goal configuration.

For concentric tubes, the rapidly exploring roadmap [196], [197] combined PRMs [194] and RRTs [195]. Later works in [205] and [206] used a rapidly exploring random graph to plan the motion interactively with the surgeon. Other methods for motion planning for continuum robots include advances to the PRM [200] and RRT [201] approaches. Recent advances with the RRT include a risk-based optimization [202], RRT* with consideration to avoid unstable configurations [129] and smoothing [203], RRTs with shape constraint [204], and multiple independent RRTs (MIRRTs) [205].

In addition to sample-based planning, other methods were developed for motion planning for concentric tube robots. These include backward average neural dynamic planning [206] and a particle swarm optimization [207].

V. OPEN CHALLENGES AND FUTURE APPLICATIONS

Almost all clinically available medical robots are rigid-link designs comparable to Fig. 4(a). The maturity and simplicity of rigid-link robot technology have facilitated their commercialization for medical applications. In contrast, the inherent flexibility and remote actuation of continuum robots present substantially greater challenges that have only been seriously studied in the last 15 years. As illustrated in Fig. 3, however, there are many existing medical devices that employ manual versions of continuum robot architectures. This indicates that, once the technological challenges have been fully addressed, the potential adoption and growth of continuum robots in medicine greatly exceeds that of rigid robots. Application areas include endoluminal, endovascular, natural orifice surgery, and deep field minimally invasive surgery.

The number of clinical-tested continuum robots (Stereotaxis, Intuitive Surgical, Auris Health (J&J), and Titan Medical) continues to grow suggesting that a tipping point in the commercialization of continuum medical robots is in the not-too-distant future. The technological challenges that must be overcome to reach this point can be summarized as follows.

A. Design and Modeling

Research to date has largely been performed in an *ad hoc* fashion. Because many of these robot designs are relatively new, researchers have tended to specialize in one continuum architecture. This has resulted in architecture-specific design and modeling techniques that are hard to generalize. This approach has also made it difficult to compare the capabilities of architectures to determine which might be best for a specific medical application. Only recently have researchers started to turn their attention to developing unifying design and modeling techniques that span all families of continuum robot morphologies. Continued work on this topic will be very important for the technology to reach the maturity level required for easy commercialization and will be critical in training the Ph.D.'s who are needed by companies at the early stages of commercialization.

B. Sensing and Control

In contrast to rigid-link robots, model-based control is extremely challenging in continuum robots. There is a high level of uncertainty in the material properties associated with robot flexure and in the modeling of transmission friction, hysteresis, and dead band. As a result, these robots are typically teleoperated, and the user must actively compensate for controller error using image feedback.

While significant progress has been made, higher fidelity methods of sensing and estimation will be needed to achieve a commercially viable level of accuracy and robustness with respect to position and force control. Developing methods for calibration and online identification of model parameters with minimal sensing requirements is the first step toward improved model-based control, and more work in this area is needed for continuum and soft robots. Additional progress can be made by refining model-based estimation techniques for force and shape.

Model-based approaches have their limits, however, and the integration of sensors into the robot body or into a sensing skin that can estimate robot shape, contact locations, and contact forces on the surrounding tissue should be a focus area of future research. Although the flexure and small cross section of continuum designs make sensor integration challenging, this is a solvable challenge that should be addressed by the research community. Once these sensing and estimation methods are mature, the control capabilities of continuum robots will rival that of rigid-link robots with substantially less invasiveness.

C. Clinical Translation

In clinical translation, the fact that many existing medical devices use manually actuated continuum architectures is a double-edged sword. On the one hand, a robotic version of an existing instrument can be more readily adopted by the medical community because it is not likely to require a substantial amount of retraining for practicing clinicians. On the other hand, the existence of a similar manual procedure, which has often been refined over decades of clinical use, creates a daunting performance benchmark in terms of procedure times, cost, and patient outcomes. Such a benchmark can be challenging to meet or exceed using the first generation of a new robot.

While the robotic instrument will almost always provide smoother and more dexterous motion than the manual version, this is unlikely to add sufficient value to justify its use. An alternative approach that has proven successful both in manufacturing and medicine is to view the robot as one part of a system. Such a system can integrate preoperative and intraoperative imaging, algorithms for procedural planning, data visualization, and assistive guidance. While some of these individual technologies are relatively mature, research challenges can arise during integration. Furthermore, such integration creates a platform for the research and development of autonomous capabilities. Continuum robotic systems of this type hold the potential to improve patient outcomes, reduce medical errors, and so justify their cost. Close collaboration between the robotics and clinical communities will be needed to reach this goal.

VI. CONCLUSION

Compared to open surgery, minimally invasive surgery can reduce patient discomfort, hasten recovery, and lower costs. While existing manual tools can enable minimally invasive access, they do not provide the level of tip dexterity and maneuverability achieved during open surgery and require substantial training. The robotics community has responded to this need by creating surgical robots with the goal of enabling the surgeon to retain the dexterity of open procedures but in the context of a minimally invasive system.

Most initial medical robots were based on rigid-link discrete-jointed industrial designs and so have been limited to line-of-site access to the incision, thereby restricting reach into the anatomy. To overcome this constraint, the medical robotics community took inspiration from manually steerable medical instruments and created robotic versions of these devices. In contrast to industrial robots, these continuum robots use flexure to modulate their shape and tip position and thereby can follow tortuous paths into the anatomy.

While industrial robots are technologically mature, continuum robot technology continues to evolve. Mechanism design, modeling, control, planning, and estimation all present unique challenges when applied to continuum robots. In this article, we have summarized the state-of-the-art of continuum robot architectures and their underlying technologies in the context of specific clinical applications. We have also identified the open research challenges and translation strategies to be addressed to achieve their widespread clinical use. ■

REFERENCES

[1] T. Kato, I. Okumura, S. Song, A. J. Golby, and N. Hata, "Tendon-driven continuum robot for endoscopic surgery: Preclinical development and validation of a tension propagation model," *IEEE/ASME Trans. Mechatronics*, vol. 20, no. 5, pp. 2252–2263, Oct. 2015.

[2] K. Xu and N. Simaan, "Analytic formulation for kinematics, statics, and shape restoration of multibackbone continuum robots via elliptic integrals," *J. Mech. Robot.*, vol. 2, no. 1, Feb. 2010, Art. no. 011006.

[3] P. E. Dupont, J. Lock, B. Itkowitz, and E. Butler, "Design and control of concentric-tube robots," *IEEE Trans. Robot.*, vol. 26, no. 2, pp. 209–225, Dec. 2010.

[4] D. C. Rucker, R. J. Webster, III, G. S. Chirikjian, and N. J. Cowan, "Equilibrium conformations of concentric-tube continuum robots," *Int. J. Robot. Res.*, vol. 29, no. 10, pp. 1263–1280, 2010.

[5] C. Bergeles, A. H. Gosline, N. V. Vasilyev, P. J. Codd, P. J. del Nido, and P. E. Dupont, "Concentric tube robot design and optimization based on task and anatomical constraints," *IEEE Trans. Robot.*, vol. 31, no. 1, pp. 67–84, Feb. 2015.

[6] Z. Mitros, M. Khadem, C. Seneci, S. Ourselin, L. Da Cruz, and C. Bergeles, "Towards modelling multi-arm robots: Eccentric arrangement of concentric tubes," in *Proc. 7th IEEE Int. Conf. Biomed. Robot. Biomechatronics (Biorob)*, Aug. 2018, pp. 43–48.

[7] J. Wang, J. Ha, and P. E. Dupont, "Steering a multi-armed robotic sheath using eccentric precurved tubes," in *Proc. Int. Conf. Robot. Automat. (ICRA)*, May 2019, pp. 9834–9840.

[8] J. Wang, J. Peine, and P. E. Dupont, "Eccentric tube robots as multiarmed steerable sheaths," *IEEE Trans. Robot.*, early access, Jun. 15, 2021, doi: 10.1109/TRO.2021.3080659.

[9] D. C. Meeker, E. H. Maslen, R. C. Ritter, and F. M. Creighton, "Optimal realization of arbitrary forces in a magnetic stereotaxis system," *IEEE Trans. Magn.*, vol. 32, no. 2, pp. 320–328, Mar. 1996.

[10] C. Heunis, J. Sikorski, and S. Misra, "Flexible instruments for endovascular interventions: Improved magnetic steering, actuation, and image-guided surgical instruments," *IEEE Robot. Autom. Mag.*, vol. 25, no. 3, pp. 71–82, Sep. 2018.

[11] T. Liu, N. L. Poirot, D. Franson, N. Seiberlich, M. A. Griswold, and M. Çavuşoğlu, "Modeling and validation of the three-dimensional deflection of an MRI-compatible magnetically actuated steerable catheter," *IEEE Trans. Biomed. Eng.*, vol. 63, no. 10, pp. 2142–2154, Oct. 2016.

[12] *Da Vinci Surgical System, Instrument and Accessory Catalog*. Accessed: Oct. 15, 2021. [Online]. Available: http://www.unthsc.edu/patient-care/wp-content/uploads/sites/27/Intuitive_Surgical_ins_cat_1_.pdf

[13] J. Lee *et al.*, "Modeling and control of robotic surgical platform for single-port access surgery," in *Proc. IEEE/RSJ Int. Conf. Intell. Robots Syst.*, Sep. 2014, pp. 3489–3495.

[14] Titan Medical. *Enos Surgical System*. Accessed: Oct. 15, 2021. [Online]. Available: https://titanmedicalinc.com/technology

[15] N. V. Vasilyev *et al.*, "Tissue removal inside the beating heart using a robotically delivered metal MEMS tool," *Int. J. Robot. Res.*, vol. 34, no. 2, pp. 236–247, Feb. 2015.

[16] K. Suzumori, S. Iikura, and H. Tanaka, "Development of flexible microactuator and its applications to robotic mechanisms," in *Proc. IEEE Int. Conf. Robot. Automat.*, Apr. 1991, pp. 1622–1623.

[17] K. Ikuta, H. Ichikawa, and K. Suzuki, "Safety-active catheter with multiple-segments driven by micro-hydraulic actuators," in *Proc. Int. Conf. Med. Image Comput. Comput.-Assist. Intervent.* Berlin, Germany: Springer, 2002, pp. 182–191.

[18] M. Cianchetti *et al.*, "Soft robotics technologies to address shortcomings in today's minimally invasive surgery: The STIFF-FLOP approach," *Soft Robot.*, vol. 1, no. 2, pp. 122–131, 2014.

[19] H. Heimberger, "Flexible endoscopic viewing tube," GB Patent 29 651 2A, Sep. 6, 1928.

[20] F. J. Wallace, "Catheter," U.S. Patent 2 688 329, Sep. 7, 1954.

[21] J. W. P. Bazinet, "Flexible tubular structures," U.S. Patent 3 162 214, Dec. 22, 1964.

[22] R. Gastroscopes and C. Schranz, "Improvements in gastroscopes and other instruments for examining tubes and cavities in the human and other bodies," GB Patent 54 846 2A, Oct. 12, 1942.

[23] T. H. O. Almen, "Medical probe for injecting X-ray contrast medium into the body," U.S. Patent 3 500 820, Mar. 17, 1970.

[24] W. A. Stark and D. A. Raible, "Double lumen diagnostic balloon catheter," U.S. Patent 3 448 739, Jun. 10, 1969.

[25] D. B. Camarillo, *Mechanics and Control of Tendon Driven Continuum Manipulators*. Stanford, CA, USA: Stanford Univ., 2008.

[26] D. B. Camarillo, C. F. Milne, C. R. Carlson, M. R. Zinn, and J. K. Salisbury, "Mechanics modeling of tendon-driven continuum manipulators," *IEEE Trans. Robot.*, vol. 24, no. 6, pp. 1262–1273, Dec. 2008.

[27] D. B. Camarillo, C. R. Carlson, and J. K. Salisbury, "Configuration tracking for continuum manipulators with coupled tendon drive," *IEEE Trans. Robot.*, vol. 25, no. 4, pp. 798–808, Aug. 2009.

[28] C. F. Graetzel, A. Sheehy, and D. P. Noonan, "Robotic bronchoscopy drive mode of the auris monarch platform*," in *Proc. Int. Conf. Robot. Automat. (ICRA)*, May 2019, pp. 3895–3901.

[29] A. Degani, H. Choset, A. Wolf, and M. A. Zenati, "Highly articulated robotic probe for minimally invasive surgery," in *Proc. IEEE Int. Conf. Robot. Automat. (ICRA)*, May 2006, pp. 4167–4172.

[30] M. Remacle, V. M. N. Prasad, G. Lawson, L. Plisson, V. Bachy, and S. Van Der Vorst, "Transoral robotic surgery (TORS) with the medrobotics flex system: First surgical application on humans," *Eur. Arch. Oto-Rhino-Laryngol.*, vol. 272, no. 6, pp. 1451–1455, Jun. 2015.

[31] N. Simaan, R. Taylor, and P. Flint, "A dexterous system for laryngeal surgery," in *Proc. IEEE Int. Conf. Robot. Automat. (ICRA)*, Apr./May 2004, pp. 351–357.

[32] S. Okazawa, R. Ebrahimi, J. Chuang, S. E. Salcudean, and R. Rohling, "Hand-held steerable needle device," *IEEE/ASME Trans. Mechatronics*, vol. 10, no. 3, pp. 285–296, Jun. 2005.

[33] P. Sears and P. Dupont, "A steerable needle technology using curved concentric tubes," in *Proc. IEEE/RSJ Int. Conf. Intell. Robots Syst.*, Oct. 2006, pp. 2850–2856.

[34] R. J. Webster, III, A. Okamura, and N. Cowan, "Toward active cannulas: Miniature snake-like surgical robots," in *Proc. IEEE/RSJ Int. Conf. Intell. Robots Syst.*, Oct. 2006, pp. 2857–2863.

[35] J. Lock, G. Laing, M. Mahvash, and P. E. Dupont, "Quasistatic modeling of concentric tube robots with external loads," in *Proc. IEEE/RSJ Int. Conf. Intell. Robots Syst.*, Oct. 2010, pp. 2325–2332.

[36] D. C. Rucker, B. A. Jones, and R. J. Webster, III, "A geometrically exact model for externally loaded concentric-tube continuum robots," *IEEE Robot. Automat. Soc.*, vol. 26, no. 5, pp. 769–780, May 2010.

[37] F. Carpi and C. Pappone, "Stereotaxis Niobe magnetic navigation system for endocardial catheter ablation and gastrointestinal capsule endoscopy," *Expert Rev. Med. Devices*, vol. 6, no. 5, pp. 487–498, Sep. 2009.

[38] E. S. Gang *et al.*, "Dynamically shaped magnetic fields: Initial animal validation of a new remote electrophysiology catheter guidance and control system," *Circulation, Arrhythmia Electrophysiol.*, vol. 4, no. 5, pp. 770–777, Oct. 2011.

[39] C. Chautems, A. Tonazzini, D. Floreano, and B. J. Nelson, "A variable stiffness catheter controlled with an external magnetic field," in *Proc. IEEE/RSJ Int. Conf. Intell. Robots Syst. (IROS)*, Sep. 2017, pp. 181–186.

[40] I. Tunay, "Modeling magnetic catheters in external fields," in *Proc. 26th Annu. Int. Conf. IEEE Eng. Med. Biol. Soc.*, vol. 1, Sep. 2004, pp. 2006–2009.

[41] I. Tunay, "Position control of catheters using magnetic fields," in *Proc. IEEE Int. Conf. Mechatronics (ICM)*, Jun. 2004, pp. 392–397.

[42] I. Tunay, "Spatial continuum models of rods undergoing large deformation and inflation," *IEEE Trans. Robot.*, vol. 29, no. 2, pp. 297–307, Apr. 2013.

[43] M. P. Kummer, J. J. Abbott, B. E. Kratochvil, R. Borer, A. Sengul, and B. J. Nelson, "OctoMag: An electromagnetic system for 5-DOF wireless micromanipulation," *IEEE Trans. Robot.*, vol. 26, no. 6, pp. 1006–1017, Dec. 2010.

[44] J. Edelmann, A. J. Petruska, and B. J. Nelson, "Magnetic control of continuum devices," *Int. J. Robot. Res.*, vol. 36, no. 1, pp. 68–85, 2017.

[45] M. Runciman, A. Darzi, and G. P. Mylonas, "Soft robotics in minimally invasive surgery," *Soft Robot.*, vol. 6, no. 4, pp. 423–443, Aug. 2019.

[46] T. Soyama, D. Yoshida, Y. Sakuhara, R. Morita, D. Abo, and K. Kudo, "The steerable microcatheter: A new device for selective catheterisation," *CardioVascular Intervent. Radiol.*, vol. 40, no. 6, pp. 947–952, Jun. 2017.

[47] M. A. Sherif *et al.*, "MitraClip step by step; how to simplify the procedure," *Netherlands Heart J.*, vol. 25, no. 2, pp. 125–130, Feb. 2017.

[48] M. Buscarini and M. Conlin, "Update on flexible ureteroscopy," *Urologia Internationalis*, vol. 80, no. 1, pp. 1–7, 2008.

[49] S. Proietti *et al.*, "The 'body mass index' of flexible ureteroscopes," *J. Endourol.*, vol. 31, no. 10, pp. 1090–1095, 2017.

[50] Intuitive Surgical Inc. *Ion Endoluminal Platform*. Accessed: Oct. 15, 2021. [Online]. Available: https://www.intuitive.com/en-us/products-and-

services/ion

[51] Auris Health. *Monarch(R) Platform*. Accessed: Oct. 15, 2021. [Online]. Available: https://www.aurishealth.com/

[52] Olympus. *Ultrathin Bronchoscope Model BF-MP190F*. Accessed: Oct. 15, 2021. [Online]. Available: https://www.olympus-europa.com/medical/en/Products-and-Solutions/Products/Product/BF-MP190F.html

[53] C. C. Smitson, L. Ang, R. Reeves, M. Patel, E. Mahmud, and A. Pourdjabbar, "Safety and feasibility of a novel, second-generation robotic-assisted system for percutaneous coronary intervention: First-in-human report," *J. Invasive Cardiol.*, vol. 30, no. 4, pp. 152–156, 2018.

[54] S. Misra, K. B. Reed, B. W. Schafer, K. T. Ramesh, and A. M. Okamura, "Mechanics of flexible needles robotically steered through soft tissue," *Int. J. Robot. Res.*, vol. 29, no. 13, pp. 1640–1660, Nov. 2010.

[55] N. J. van de Berg, D. J. van Gerwen, J. Dankelman, and J. J. van den Dobbelsteen, "Design choices in needle steering—A review," *IEEE/ASME Trans. Mechatronics*, vol. 20, no. 5, pp. 2172–2183, Oct. 2015.

[56] G. Ciuti *et al.*, "Frontiers of robotic colonoscopy: A comprehensive review of robotic colonoscopes and technologies," *J. Clin. Med.*, vol. 9, no. 6, p. 1648, May 2020.

[57] B. Seeliger, M. Diana, J. P. Ruurda, K. M. Konstantinidis, J. Marescaux, and L. L. Swanström, "Enabling single-site laparoscopy: The SPORT platform," *Surgical Endoscopy*, vol. 33, no. 11, pp. 3696–3703, Nov. 2019.

[58] K. Xu, R. E. Goldman, J. Ding, P. K. Allen, D. L. Fowler, and N. Simaan, "System design of an insertable robotic effector platform for single port access (SPA) surgery," in *Proc. IEEE/RSJ Int. Conf. Intell. Robots Syst.*, Oct. 2009, pp. 5546–5552.

[59] N. Simaan, A. Bajo, A. Reiter, L. Wang, P. Allen, and D. Fowler, "Lessons learned using the insertable robotic effector platform (IREP) for single port access surgery," *J. Robot. Surg.*, vol. 7, no. 3, pp. 235–240, Sep. 2013.

[60] K. Xu, M. Fu, and J. Zhao, "Design of the SJTU unfoldable robotic system (SURS) for single port laparoscopy," in *Proc. IEEE Int. Conf. Robot. Biomimetics (ROBIO)*, Dec. 2014, pp. 53–57.

[61] K. Xu, J. Zhao, and M. Fu, "Development of the SJTU unfoldable robotic system (SURS) for single port laparoscopy," *IEEE/ASME Trans. Mechatronics*, vol. 20, no. 5, pp. 2133–2145, Oct. 2015.

[62] A. Orekhov, C. Abah, and N. Simaan, "Snake-like robots for minimally invasive, single-port, and intraluminal surgeries," in *The Encyclopedia of Medical Robotics*. Singapore: World Scientific, 2018, pp. 203–243.

[63] R. Bertolo, J. Garisto, M. Gettman, and J. Kaouk, "Novel system for robotic single-port surgery: Feasibility and state of the art in urology," *Eur. Urol. Focus*, vol. 4, no. 5, pp. 669–673, Sep. 2018.

[64] N. Sarli, G. D. Giudice, S. De, M. S. Dietrich, S. D. Herrell, and N. Simaan, "TURBot: A system for robot-assisted transurethral bladder tumor resection," *IEEE/ASME Trans. Mechatronics*, vol. 24, no. 4, pp. 1452–1463, Aug. 2019.

[65] J. Zhao, X. Zheng, M. Zheng, A. J. Shih, and K. Xu, "An endoscopic continuum testbed for finalizing system characteristics of a surgical robot for NOTES procedures," in *Proc. IEEE/ASME Int. Conf. Adv. Intell. Mechatronics*, Jul. 2013, pp. 63–70.

[66] F. Risi, "Considerations and rationale for cochlear implant electrode design-past, present and future," *J. Int. Adv. Otol.*, vol. 14, no. 3, p. 382, 2018.

[67] T. Lenarz, T. Stöver, A. Buechner, A. Lesinski-Schiedat, J. Patrick, and J. Pesch, "Hearing conservation surgery using the hybrid-L electrode," *Audiol. Neurotol.*, vol. 14, no. 1, pp. 22–31, 2009.

[68] J. Zhang, W. Wei, J. Ding, J. T. Roland, Jr., S. Manolidis, and N. Simaan, "Inroads toward robot-assisted cochlear implant surgery using steerable electrode arrays," *Otol. Neurotol.*, vol. 31, no. 8, pp. 1199–1206, 2010.

[69] J. Zhang and N. Simaan, "Design of underactuated steerable electrode arrays for optimal insertions," *J. Mech. Robot.*, vol. 5, no. 1, Feb. 2013, Art. no. 011008.

[70] T. L. Bruns *et al.*, "Magnetically steered robotic insertion of cochlear-implant electrode arrays: System integration and first-in-cadaver results," *IEEE Robot. Autom. Lett.*, vol. 5, no. 2, pp. 2240–2247, Apr. 2020.

[71] L. Leon, F. M. Warren, and J. J. Abbott, "An *in-vitro* insertion-force study of magnetically guided lateral-wall cochlear-implant electrode arrays," *Otol. Neurotol.*, vol. 39, no. 2, pp. e63–e73, 2018.

[72] H. Carmichael, A. P. D'Andrea, M. Skancke, V. Obias, and P. Sylla, "Feasibility of transanal total mesorectal excision (taTME) using the medrobotics flex system," *Surgical Endoscopy*, vol. 34, no. 1, pp. 485–491, Jan. 2020.

[73] P. Berthet-Rayne *et al.*, "The i^2 snake robotic platform for endoscopic surgery," *Ann. Biomed. Eng.*, vol. 46, no. 10, pp. 1663–1675, 2018.

[74] T. Ota *et al.*, "A novel highly articulated robotic surgical system for epicardial ablation," in *Proc. 30th Annu. Int. Conf. IEEE Eng. Med. Biol. Soc.*, Aug. 2008, pp. 250–253.

[75] Z. Li and C. S. Ng, "Future of uniportal video-assisted thoracoscopic surgery—Emerging technology," *Ann. Cardiothoracic Surg.*, vol. 5, no. 2, p. 127, 2016.

[76] J. J. Rassweiler *et al.*, "Future of robotic surgery in urology," *BJU Int.*, vol. 120, no. 6, pp. 822–841, Dec. 2017.

[77] J. Ding, R. E. Goldman, K. Xu, P. K. Allen, D. L. Fowler, and N. Simaan, "Design and coordination kinematics of an insertable robotic effectors platform for single-port access surgery," *IEEE/ASME Trans. Mechatronics*, vol. 18, no. 5, pp. 1612–1624, Oct. 2013.

[78] K. Groom, L. Wang, N. Simaan, and J. Netterville, "Robot-assisted transnasal laryngoplasty in cadaveric models: Quantifying forces and identifying challenges," *Laryngoscope*, vol. 125, no. 5, pp. 1166–1168, May 2015.

[79] N. Simaan, "Design and integration of a telerobotic system for minimally invasive surgery of the throat," *Int. J. Robot. Res.*, vol. 28, no. 9, pp. 1134–1153, May 2009.

[80] M. F. Rox *et al.*, "Mechatronic design of a two-arm concentric tube robot system for rigid neuroendoscopy," *IEEE/ASME Trans. Mechatronics*, vol. 25, no. 3, pp. 1432–1443, Jun. 2020.

[81] J. Burgner *et al.*, "A telerobotic system for transnasal surgery," *IEEE/ASME Trans. Mechatronics*, vol. 19, no. 3, pp. 996–1006, Jun. 2014.

[82] G. Fagogenis *et al.*, "Autonomous robotic intracardiac catheter navigation using haptic vision," *Sci. Robot.*, vol. 4, no. 29, Apr. 2019, Art. no. eaaw1977.

[83] A. Agrawal, D. K. Hogarth, and S. Murgu, "Robotic bronchoscopy for pulmonary lesions: A review of existing technologies and clinical data," *J. Thoracic Disease*, vol. 12, no. 6, p. 3279, 2020.

[84] A. C. Chen and C. T. Gillespie, "Robotic endoscopic airway challenge: REACH assessment," *Ann. Thoracic Surg.*, vol. 106, no. 1, pp. 293–297, Jul. 2018.

[85] *Olympus*. Accessed: Oct. 15, 2021. [Online]. Available: https://www.olympus-europa.com/medical/rmt/media/en/Content/Content-MSD/Documents/Brochures/SRP-Periphery/E0428337EN_EEIII_BF-MP190_A4_EN.pdf

[86] C. Chautems, S. Lyttle, Q. Boehler, and B. J. Nelson, "Design and evaluation of a steerable magnetic sheath for cardiac ablations," *IEEE Robot. Autom. Lett.*, vol. 3, no. 3, pp. 2123–2128, Jul. 2018.

[87] A. P. Mamunes *et al.*, "Magnetic flexible endoscope for colonoscopy: An initial learning curve analysis," *Endoscopy Int. Open*, vol. 9, no. 2, pp. E171–E180, Feb. 2021.

[88] P. R. Slawinski *et al.*, "Autonomously controlled magnetic flexible endoscope for colon exploration," *Gastroenterology*, vol. 154, no. 6, pp. 1577–1579, Mar. 2018.

[89] M. P. Armacost *et al.*, "Accurate and reproducible target navigation with the stereotaxis Niobe magnetic navigation system," *J. Cardiovascular Electrophysiol.*, vol. 18, pp. S26–S31, Jan. 2007.

[90] B. L. Nguyen, J. L. Merino, and E. S. Gang, "Remote navigation for ablation procedures—A new step forward in the treatment of cardiac arrhythmias," *Eur. Cardiol.*, vol. 6, no. 3, pp. 50–56, 2010.

[91] S. Tully, G. Kantor, M. A. Zenati, and H. Choset, "Shape estimation for image-guided surgery with a highly articulated snake robot," in *Proc. IEEE/RSJ Int. Conf. Intell. Robots Syst.*, Sep. 2011, pp. 1353–1358.

[92] V. Y. Reddy *et al.*, "View-synchronized robotic image-guided therapy for atrial fibrillation ablation: Experimental validation and clinical feasibility," *Circulation*, vol. 115, no. 21, pp. 2705–2714, May 2007.

[93] A. Al-Ahmad, J. D. Grossman, and P. J. Wang, "Early experience with a computerized robotically controlled catheter system," *J. Interventional Cardiac Electrophysiol.*, vol. 12, no. 3, pp. 199–202, Apr. 2005.

[94] E. Folch *et al.*, "A prospective, multi-center evaluation of the clinical utility of the ion endoluminal system-experience using a robotic-assisted bronchoscope system with shape-sensing technology," in *Advances in Interventional Pulmonology*. New York, NY, USA: American Thoracic Society, 2020, p. A2719.

[95] J. Reisenauer *et al.*, "Ion: Technology and techniques for shape-sensing robotic-assisted bronchoscopy," *Ann. Thoracic Surg.*, vol. 113, no. 1, pp. 308–315, Jan. 2022.

[96] P. J. Swaney *et al.*, "Design of a quadramanual robot for single-nostril skull base surgery," in *Proc. ASME DSCC/MOVIC*, 2012, pp. 387–393.

[97] M. T. Chikhaoui, J. Granna, J. Starke, and J. Burgner-Kahrs, "Toward motion coordination control and design optimization for dual-arm concentric tube continuum robots," *IEEE Robot. Autom. Lett.*, vol. 3, no. 3, pp. 1793–1800, Jul. 2018.

[98] X. Yang, S. Song, L. Liu, T. Yan, and M. Q.-H. Meng, "Design and optimization of concentric tube robots based on surgical tasks, anatomical constraints and follow-the-leader deployment," *IEEE Access*, vol. 7, pp. 173612–173625, 2019.

[99] P. I. Corke, "A simple and systematic approach to assigning Denavit–Hartenberg parameters," *IEEE Trans. Robot.*, vol. 23, no. 3, pp. 590–594, Jun. 2007.

[100] K. M. Lynch and F. C. Park, *Modern Robotics*. Cambridge, U.K.: Cambridge Univ. Press, 2017.

[101] R. J. Webster, III, and B. A. Jones, "Design and kinematic modeling of constant curvature continuum robots: A review," *Int. J. Robot. Res.*, vol. 29, no. 13, pp. 1661–1683, 2010.

[102] J. A. Childs and C. Rucker, "Concentric precurved bellows: New bending actuators for soft robots," *IEEE Robot. Autom. Lett.*, vol. 5, no. 2, pp. 1215–1222, Apr. 2020.

[103] A. Chawla, C. Frazelle, and I. Walker, "A comparison of constant curvature forward kinematics for multisection continuum manipulators," in *Proc. 2nd IEEE Int. Conf. Robot. Comput. (IRC)*, Jan. 2018, pp. 217–223.

[104] C. D. Santina, A. Bicchi, and D. Rus, "On an improved state parametrization for soft robots with piecewise constant curvature and its use in model based control," *IEEE Robot. Autom. Lett.*, vol. 5, no. 2, pp. 1001–1008, Apr. 2020.

[105] T. F. Allen, L. Rupert, T. R. Duggan, G. Hein, and K. Albert, "Closed-form non-singular constant-curvature continuum manipulator kinematics," in *Proc. 3rd IEEE Int. Conf. Soft Robot. (RoboSoft)*, May 2020, pp. 410–416.

[106] F. Renda, F. Boyer, J. Dias, and L. Seneviratne, "Discrete cosserat approach for multisection soft manipulator dynamics," *IEEE Trans. Robot.*, vol. 34, no. 6, pp. 1518–1533, Dec. 2018.

[107] S. Neppalli, M. A. Csencsits, B. A. Jones, and I. Walker, "A geometrical approach to inverse kinematics for continuum manipulators," in *Proc. IEEE/RSJ Int. Conf. Intell. Robots Syst.*, Sep. 2008, pp. 3565–3570.

[108] K. Xu and N. Simaan, "Intrinsic wrench estimation and its performance index for multisegment continuum robots," *IEEE Trans. Robot.*, vol. 26, no. 3, pp. 555–561, Jun. 2010.

[109] F. Boyer, V. Lebastard, F. Candelier, and F. Renda, "Dynamics of continuum and soft robots: A strain parameterization based approach," *IEEE Trans. Robot.*, vol. 37, no. 3, pp. 847–863, Jun. 2021.

[110] D. C. Rucker and R. J. Webster, III, "Statics and dynamics of continuum robots with general tendon routing and external loading," *IEEE Trans. Robot.*, vol. 27, no. 6, pp. 1033–1044, Dec. 2011.

[111] M. Hannan and I. Walker, "Vision based shape estimation for continuum robots," in *Proc. IEEE Int. Conf. Robot. Automat.*, Sep. 2003, pp. 3449–3454.

[112] M. M. Dalvand, S. Nahavandi, and R. D. Howe, "An analytical loading model for n-tendon continuum robots," *IEEE Trans. Robot.*, vol. 34, no. 5, pp. 1215–1225, Oct. 2018.

[113] K. Oliver-Butler, J. Till, and C. Rucker, "Continuum robot stiffness under external loads and prescribed tendon displacements," *IEEE Trans. Robot.*, vol. 35, no. 2, pp. 403–419, Apr. 2019.

[114] J. Jung, R. S. Penning, and M. R. Zinn, "A modeling approach for robotic catheters: Effects of nonlinear internal device friction," *Adv. Robot.*, vol. 28, no. 8, pp. 557–572, Apr. 2014.

[115] Y. Liu and F. Alambeigi, "Effect of external and internal loads on tension loss of tendon-driven continuum manipulators," *IEEE Robot. Autom. Lett.*, vol. 6, no. 2, pp. 1606–1613, Apr. 2021.

[116] M. T. Chikhaoui, S. Lilge, S. Kleinschmidt, and J. Burgner-Kahrs, "Comparison of modeling approaches for a tendon actuated continuum robot with three extensible segments," *IEEE Robot. Autom. Lett.*, vol. 4, no. 2, pp. 989–996, Apr. 2019.

[117] R. A. Srivatsan, M. Travers, and H. Choset, "Using lie algebra for shape estimation of medical snake robots," in *Proc. IEEE/RSJ Int. Conf. Intell. Robots Syst.*, Sep. 2014, pp. 3483–3488.

[118] K. Xu and N. Simaan, "An investigation of the intrinsic force sensing capabilities of continuum robots," *IEEE Trans. Robot.*, vol. 24, no. 3, pp. 576–587, Jun. 2008.

[119] R. Roy, L. Wang, and N. Simaan, "Investigation of effects of dynamics on intrinsic wrench sensing in continuum robots," in *Proc. IEEE Int. Conf. Robot. Automat. (ICRA)*, May 2016, pp. 2052–2059.

[120] N. Simaan, "Snake-like units using flexible backbones and actuation redundancy for enhanced miniaturization," in *Proc. IEEE Int. Conf. Robot. Automat.*, Barcelona, Spain, Apr. 2005, pp. 3012–3017.

[121] K. Xu and N. Simaan, "Analytic formulation for kinematics, statics, and shape restoration of multibackbone continuum robots via elliptic integrals," *ASME J. Mech. Robot.*, vol. 2, no. 1, pp. 11006–11013, Feb. 2010.

[122] A. L. Orekhov, V. A. Aloi, and D. C. Rucker, "Modeling parallel continuum robots with general intermediate constraints," in *Proc. IEEE Int. Conf. Robot. Automat. (ICRA)*, May 2017, pp. 6142–6149.

[123] Y. Chen, B. Wu, J. Jin, and K. Xu, "A variable curvature model for multi-backbone continuum robots to account for inter-segment coupling and external disturbance," *IEEE Robot. Autom. Lett.*, vol. 6, no. 2, pp. 1590–1597, Apr. 2021.

[124] P. E. Dupont, J. Lock, and E. Butler, "Torsional kinematic model for concentric tube robots," in *Proc. IEEE Int. Conf. Robot. Automat.*, May 2009, pp. 3851–3858.

[125] R. J. Webster, III, J. M. Romano, and N. J. Cowan, "Mechanics of precurved-tube continuum robots," *IEEE Trans. Robot.*, vol. 25, no. 1, pp. 67–78, Feb. 2009.

[126] J. Till, V. Aloi, K. E. Riojas, P. L. Anderson, R. J. Webster, III, and C. Rucker, "A dynamic model for concentric tube robots," *IEEE Trans. Robot.*, vol. 36, no. 6, pp. 1704–1718, Dec. 2020.

[127] H. B. Gilbert, R. J. Hendrick, and R. J. Webster, III, "Elastic stability of concentric tube robots: A stability measure and design test," *IEEE Trans. Robot.*, vol. 32, no. 1, pp. 20–35, Feb. 2016.

[128] J. Ha, F. C. Park, and P. E. Dupont, "Elastic stability of concentric tube robots subject to external loads," *IEEE Trans. Biomed. Eng.*, vol. 63, no. 6, pp. 1116–1128, Jun. 2016.

[129] C. Bergeles and P. E. Dupont, "Planning stable paths for concentric tube robots," in *Proc. IEEE/RSJ Int. Conf. Intell. Robots Syst.*, Nov. 2013, pp. 3077–3082.

[130] K. Leibrandt, C. Bergeles, and G.-Z. Yang, "On-line collision-free inverse kinematics with frictional active constraints for effective control of unstable concentric tube robots," in *Proc. IEEE/RSJ Int. Conf. Intell. Robots Syst. (IROS)*, Sep. 2015, pp. 3797–3804.

[131] M. Khadem, J. O'Neill, Z. Mitros, L. D. Cruz, and C. Bergeles, "Autonomous steering of concentric tube robots for enhanced force/velocity manipulability," in *Proc. IEEE/RSJ Int. Conf. Intell. Robots Syst. (IROS)*, Nov. 2019, pp. 2197–2204.

[132] C. Girerd, K. Rabenorosoa, P. Rougeot, and P. Renaud, "Towards optical biopsy of olfactory cells using concentric tube robots with follow-the-leader deployment," in *Proc. IEEE/RSJ Int. Conf. Intell. Robots Syst. (IROS)*, Sep. 2017, pp. 5661–5887.

[133] M. Khadem, J. O'Neill, Z. Mitros, L. da Cruz, and C. Bergeles, "Autonomous steering of concentric tube robots via nonlinear model predictive control," *IEEE Trans. Robot.*, vol. 36, no. 5, pp. 1595–1602, Oct. 2020.

[134] C. Girerd, A. V. Kudryavtsev, P. Rougeot, P. Renaud, K. Rabenorosoa, and B. Tamadazte, "SLAM-based follow-the-leader deployment of concentric tube robots," *IEEE Robot. Autom. Lett.*, vol. 5, no. 2, pp. 548–555, Apr. 2020.

[135] T. L. Bruns *et al.*, "A modular, multi-arm concentric tube robot system with application to transnasal surgery for orbital tumors," *Int. J. Robot. Res.*, vol. 40, nos. 2–3, pp. 521–533, Feb. 2021.

[136] J. Ha, F. C. Park, and P. E. Dupont, "Achieving elastic stability of concentric tube robots through optimization of tube precurvature," in *Proc. IEEE/RSJ Int. Conf. Intell. Robots Syst.*, Sep. 2014, pp. 864–870.

[137] R. J. Hendrick, H. B. Gilbert, and R. J. Webster, III, "Designing snap-free concentric tube robots: A local bifurcation approach," in *Proc. IEEE Int. Conf. Robot. Automat. (ICRA)*, May 2015, pp. 2256–2263.

[138] M. Boushaki, C. Liu, B. Herman, V. Trevillot, M. Akkari, and P. Poignet, "Optimization of concentric-tube robot design for deep anterior brain tumor surgery," in *Proc. 14th Int. Conf. Control, Automat., Robot. Vis. (ICARCV)*, Nov. 2016, pp. 1–6.

[139] J. Ha and P. E. Dupont, "Designing stable concentric tube robots using piecewise straight tubes," *IEEE Robot. Autom. Lett.*, vol. 2, no. 1, pp. 298–304, Jan. 2017.

[140] J. Ha, F. C. Park, and P. E. Dupont, "Optimizing tube precurvature to enhance the elastic stability of concentric tube robots," *IEEE Trans. Robot.*, vol. 33, no. 1, pp. 22–37, Feb. 2017.

[141] J. Lock and P. E. Dupont, "Friction modeling in concentric tube robots," in *Proc. IEEE Int. Conf. Robot. Automat.*, May 2011, pp. 1139–1146.

[142] J. Ha and P. E. Dupont, "Incorporating tube-to-tube clearances in the kinematics of concentric tube robots," in *Proc. IEEE Int. Conf. Robot. Automat. (ICRA)*, May 2017, pp. 6730–6736.

[143] J. Ha, G. Fagogenis, and P. E. Dupont, "Modeling tube clearance and bounding the effect of friction in concentric tube robot kinematics," *IEEE Trans. Robot.*, vol. 35, no. 2, pp. 353–370, Apr. 2019.

[144] J. J. Abbott, E. Diller, and A. J. Petruska, "Magnetic methods in robotics," *Annu. Rev. Control, Robot., Auton. Syst.*, vol. 3, no. 1, pp. 57–90, May 2020.

[145] L. B. Kratchman, T. L. Bruns, J. J. Abbott, and R. J. Webster, III, "Guiding elastic rods with a robot-manipulated magnet for medical applications," *IEEE Trans. Robot.*, vol. 33, no. 1, pp. 227–233, Feb. 2017.

[146] Q. Peyron, Q. Boehler, K. Rabenorosoa, B. J. Nelson, P. Renaud, and N. Andreff, "Kinematic analysis of magnetic continuum robots using continuation method and bifurcation analysis," *IEEE Robot. Autom. Lett.*, vol. 3, no. 4, pp. 3646–3653, Oct. 2018.

[147] D. Trivedi, C. D. Rahn, W. M. Kier, and I. D. Walker, "Soft robotics: Biological inspiration, state of the art, and future research," *Appl. Bionics Biomech.*, vol. 5, no. 3, pp. 99–117, Sep. 2008.

[148] C. D. Santina, R. K. Katzschmann, A. Bicchi, and D. Rus, "Model-based dynamic feedback control of a planar soft robot: Trajectory tracking and interaction with the environment," *Int. J. Robot. Res.*, vol. 39, no. 4, pp. 490–513, Mar. 2020.

[149] K. M. Digumarti, A. T. Conn, and J. Rossiter, "Euglenoid-inspired giant shape change for highly deformable soft robots," *IEEE Robot. Autom. Lett.*, vol. 2, no. 4, pp. 2302–2307, Oct. 2017.

[150] O. Goury and C. Duriez, "Fast, generic, and reliable control and simulation of soft robots using model order reduction," *IEEE Trans. Robot.*, vol. 34, no. 6, pp. 1565–1576, Dec. 2018.

[151] Y. Adagolodjo, F. Renda, and C. Duriez, "Coupling numerical deformable models in global and reduced coordinates for the simulation of the direct and the inverse kinematics of soft robots," *IEEE Robot. Autom. Lett.*, vol. 6, no. 2, pp. 3910–3917, Apr. 2021.

[152] C. B. Black, J. Till, and D. C. Rucker, "Parallel continuum robots: Modeling, analysis, and actuation-based force sensing," *IEEE Trans. Robot.*, vol. 34, no. 1, pp. 29–47, Feb. 2018.

[153] R. M. Murray, Z. Li, and S. S. Sastry, *A Mathematical Introduction to Robotic Manipulation*. Boca Raton, FL, USA: CRC Press, 1994.

[154] J. Till, C. E. Bryson, S. Chung, A. Orekhov, and D. C. Rucker, "Efficient computation of multiple coupled cosserat rod models for real-time simulation and control of parallel continuum manipulators," in *Proc. IEEE Int. Conf. Robot. Automat. (ICRA)*, May 2015, pp. 5067–5074.

[155] D. C. Rucker and R. J. Webster, III, "Computing Jacobians and compliance matrices for externally loaded continuum robots," in *Proc. IEEE Int. Conf. Robot. Automat.*, May 2011, pp. 945–950.

[156] K. Xu and N. Simaan, "Actuation compensation for flexible surgical snake-like robots with redundant remote actuation," in *Proc. IEEE Int. Conf. Robot. Automat. (ICRA)*, May 2006, pp. 4148–4154.

[157] R. Roy, L. Wang, and N. Simaan, "Modeling and estimation of friction, extension, and coupling effects in multisegment continuum robots," *IEEE/ASME Trans. Mechatronics*, vol. 22, no. 2, pp. 909–920, Apr. 2017.

[158] A. Bajo, R. E. Goldman, and N. Simaan, "Configuration and joint feedback for enhanced performance of multi-segment continuum robots," in *Proc. IEEE Int. Conf. Robot. Automat.*, May 2011, pp. 2905–2912.

[159] F. Campisano *et al.*, "Online disturbance estimation for improving kinematic accuracy in continuum manipulators," *IEEE Robot. Autom. Lett.*, vol. 5, no. 2, pp. 2642–2649, Apr. 2020.

[160] F. Campisano *et al.*, "Closed-loop control of soft continuum manipulators under tip follower actuation," *Int. J. Robot. Res.*, vol. 40, nos. 6–7, pp. 923–938, Jun. 2021.

[161] G. J. Vrooijink, A. Denasi, J. G. Grandjean, and S. Misra, "Model predictive control of a robotically actuated delivery sheath for beating heart compensation," *Int. J. Robot. Res.*, vol. 36, no. 2, pp. 193–209, Feb. 2017.

[162] O. Khatib, "A unified approach for motion and force control of robot manipulators: The operational space formulation," *IEEE J. Robot. Autom.*, vol. RA-3, no. 1, pp. 43–53, Feb. 1987.

[163] R. Featherstone, S. S. Thiebaut, and O. Khatib, "A general contact model for dynamically-decoupled force/motion control," in

Proc. IEEE Int. Conf. Robot. Automat., vol. 4, May 1999, pp. 3281–3286.

[164] M. Mahvash and P. E. Dupont, "Stiffness control of surgical continuum manipulators," *IEEE Trans. Robot.*, vol. 27, no. 2, pp. 334–345, Apr. 2011.

[165] S. B. Kesner and R. D. Howe, "Force control of flexible catheter robots for beating heart surgery," in *Proc. IEEE Int. Conf. Robot. Automat.*, May 2011, pp. 1589–1594.

[166] A. Bajo and N. Simaan, "Hybrid motion/force control of multi-backbone continuum robots," *Int. J. Robot. Res.*, vol. 35, no. 4, pp. 422–434, Apr. 2016.

[167] R. Yasin and N. Simaan, "Joint-level force sensing for indirect hybrid force/position control of continuum robots with friction," *Int. J. Robot. Res.*, vol. 40, nos. 4–5, pp. 764–781, Apr. 2021.

[168] R. E. Goldman, A. Bajo, and N. Simaan, "Compliant motion control for multisegment continuum robots with actuation force sensing," *IEEE Trans. Robot.*, vol. 30, no. 4, pp. 890–902, Aug. 2014.

[169] M. C. Yip and D. B. Camarillo, "Model-less hybrid position/force control: A minimalist approach for continuum manipulators in unknown, constrained environments," *IEEE Robot. Autom. Lett.*, vol. 1, no. 2, pp. 844–851, Jul. 2016.

[170] Z. Lunwei, Q. Jinwu, S. Linyong, and Z. Yanan, "FBG sensor devices for spatial shape detection of intelligent colonoscope," in *Proc. IEEE Int. Conf. Robot. Automat.*, vol. 1, Apr. 2004, pp. 834–840.

[171] R. J. Roesthuis, S. Janssen, and S. Misra, "On using an array of fiber Bragg grating sensors for closed-loop control of flexible minimally invasive surgical instruments," in *Proc. IEEE/RSJ Int. Conf. Intell. Robot. Syst.*, Oct. 2013, pp. 2545–2551.

[172] H. Liu, A. Farvardin, S. A. Pedram, I. Iordachita, R. H. Taylor, and M. Armand, "Large deflection shape sensing of a continuum manipulator for minimally-invasive surgery," in *Proc. IEEE Int. Conf. Robot. Automat. (ICRA)*, May 2015, pp. 201–206.

[173] R. Xu, A. Yurkewich, and R. V. Patel, "Curvature, torsion, and force sensing in continuum robots using helically wrapped FBG sensors," *IEEE Robot. Autom. Lett.*, vol. 1, no. 2, pp. 1052–1059, Jul. 2016.

[174] Y. Shapiro, G. Kósa, and A. Wolf, "Shape tracking of planar hyper-flexible beams via embedded PVDF deflection sensors," *IEEE/ASME Trans. Mechatronics*, vol. 19, no. 4, pp. 1260–1267, Aug. 2014.

[175] B. Kim, J. Ha, F. C. Park, and P. E. Dupont, "Optimizing curvature sensor placement for fast, accurate shape sensing of continuum robots," in *Proc. IEEE Int. Conf. Robot. Automat. (ICRA)*, May 2014, pp. 5374–5379.

[176] L. Wang and N. Simaan, "Geometric calibration of continuum robots: Joint space and equilibrium shape deviations," *IEEE Trans. Robot.*, vol. 35, no. 2, pp. 387–402, Apr. 2019.

[177] A. Bajo and N. Simaan, "Finding lost wrenches: Using continuum robots for contact detection and estimation of contact location," in *Proc. IEEE Int. Conf. Robot. Automat.*, May 2010, pp. 3666–3673.

[178] A. Bajo and N. Simaan, "Kinematics-based detection and localization of contacts along multisegment continuum robots," *IEEE Trans. Robot.*, vol. 28, no. 2, pp. 291–302, Apr. 2012.

[179] Y. Chen, L. Wang, K. Galloway, I. Godage, N. Simaan, and E. Barth, "Modal-based kinematics and contact detection of soft robots," *Soft Robot.*, vol. 8, no. 3, pp. 298–309, Jun. 2021.

[180] W. Wei and N. Simaan, "Modeling, force sensing, and control of flexible cannulas for microstent delivery," *J. Dyn. Syst., Meas., Control*, vol. 134, no. 4, Jul. 2012, Art. no. 041004.

[181] D. C. Rucker and R. J. Webster, III, "Deflection-based force sensing for continuum robots: A probabilistic approach," in *Proc. IEEE/RSJ Int. Conf. Intell. Robots Syst.*, Sep. 2011, pp. 3764–3769.

[182] Q. Qiao, G. Borghesan, J. De Schutter, and E. B. V. Poorten, "Force from shape—Estimating the location and magnitude of the external force on flexible instruments," *IEEE Trans. Robot.*, vol. 37, no. 5, pp. 1826–1833, Oct. 2021.

[183] M. K. Soltani, S. Khanmohammadi, and F. Ghalichi, "A three-dimensional shape-based force and stiffness-sensing platform for tendon-driven catheters," *Sensors*, vol. 16, no. 7, p. 990, Jun. 2016.

[184] M. Khoshnam, A. C. Skanes, and R. V. Patel, "Modeling and estimation of tip contact force for steerable ablation catheters," *IEEE Trans. Biomed. Eng.*, vol. 62, no. 5, pp. 1404–1415, May 2015.

[185] S. Hasanzadeh and F. Janabi-Sharifi, "Model-based force estimation for intracardiac catheters," *IEEE/ASME Trans. Mechatronics*, vol. 21, no. 1, pp. 154–162, Feb. 2016.

[186] H. Yuan, P. W. Y. Chiu, and Z. Li, "Shape-reconstruction-based force sensing method for continuum surgical robots with large deformation," *IEEE Robot. Autom. Lett.*, vol. 2, no. 4, pp. 1972–1979, Oct. 2017.

[187] V. A. Aloi and D. C. Rucker, "Estimating loads along elastic rods," in *Proc. Int. Conf. Robot. Automat. (ICRA)*, May 2019, pp. 2867–2873.

[188] H. Donat, S. Lilge, J. Burgner-Kahrs, and J. J. Steil, "Estimating tip contact forces for concentric tube continuum robots based on backbone deflection," *IEEE Trans. Med. Robot. Bionics*, vol. 2, no. 4, pp. 619–630, Nov. 2020.

[189] J. Burgner-Kahrs, D. C. Rucker, and H. Choset, "Continuum robots for medical applications: A survey," *IEEE Trans. Robot.*, vol. 31, no. 6, pp. 1261–1280, Dec. 2015.

[190] T. Ota, A. Degani, A. Wolf, H. Choset, and M. A. Zenati, "Epicardial atrial ablation using a novel highly articulated robotic probe through a subxiphoid approach," *Amer. J. Cardiol.*, vol. 98, p. 248M, Oct. 2006.

[191] H. Alfalahi, F. Renda, and C. Stefanini, "Concentric tube robots for minimally invasive surgery: Current applications and future opportunities," *IEEE Trans. Med. Robot. Bionics*, vol. 2, no. 3, pp. 410–424, Aug. 2020.

[192] L. A. Lyons, R. J. Webster, III, and R. Alterovitz, "Motion planning for active cannulas," in *Proc. IEEE/RSJ Int. Conf. Intell. Robots Syst.*, Oct. 2009, pp. 801–806.

[193] L. A. Lyons, R. J. Webster, III, and R. Alterovitz, "Planning active cannula configurations through tubular anatomy," in *Proc. IEEE Int. Conf. Robot. Automat.*, May 2010, pp. 2082–2087.

[194] L. E. Kavraki, P. Svestka, J.-C. Latombe, and M. H. Overmars, "Probabilistic roadmaps for path planning in high-dimensional configuration spaces," *IEEE Trans. Robot. Automat.*, vol. 12, no. 4, pp. 566–580, Aug. 1996.

[195] S. M. LaValle and J. J. Kuffner, "Rapidly-exploring random trees: Progress and prospects," *Algorithmic Comput. Robot., New Directions*, vol. 5, pp. 293–308, Jul. 2001.

[196] R. Alterovitz, S. Patil, and A. Derbakova, "Rapidly-exploring roadmaps: Weighing exploration vs. Refinement in optimal motion planning," in *Proc. IEEE Int. Conf. Robot. Automat.*, May 2011, pp. 3706–3712.

[197] L. G. Torres and R. Alterovitz, "Motion planning for concentric tube robots using mechanics-based models," in *Proc. IEEE/RSJ Int. Conf. Intell. Robots Syst.*, Sep. 2011, pp. 5153–5159.

[198] L. G. Torres, C. Baykal, and R. Alterovitz, "Interactive-rate motion planning for concentric tube robots," in *Proc. IEEE Int. Conf. Robot. Automat. (ICRA)*, May 2014, pp. 1915–1921.

[199] L. G. Torres *et al.*, "A motion planning approach to automatic obstacle avoidance during concentric tube robot teleoperation," in *Proc. IEEE Int. Conf. Robot. Automat. (ICRA)*, May 2015, pp. 2361–2367.

[200] K. Leibrandt, C. Bergeles, and G.-Z. Yang, "Implicit active constraints for safe and effective guidance of unstable concentric tube robots," in *Proc. IEEE/RSJ Int. Conf. Intell. Robots Syst. (IROS)*, Oct. 2016, pp. 1157–1163.

[201] A. Kuntz *et al.*, "Motion planning for continuum reconfigurable incisionless surgical parallel robots," in *Proc. IEEE/RSJ Int. Conf. Intell. Robots Syst. (IROS)*, Sep. 2017, pp. 6463–6469.

[202] C. Caborni, S. Y. Ko, E. De Momi, G. Ferrigno, and F. R. y Baena, "Risk-based path planning for a steerable flexible probe for neurosurgical intervention," in *Proc. 4th IEEE RAS EMBS Int. Conf. Biomed. Robot. Biomechatronics (BioRob)*, Jun. 2012, pp. 866–871.

[203] D. Zhang, J. Wang, X. Yang, S. Song, and M. Q.-H. Meng, "RRT*-smooth algorithm applied to motion planning of concentric tube robots," in *Proc. IEEE Int. Conf. Inf. Automat. (ICIA)*, Aug. 2018, pp. 487–493.

[204] K. Wu, L. Wu, and H. Ren, "Motion planning of continuum tubular robots based on centerlines extracted from statistical atlas," in *Proc. IEEE/RSJ Int. Conf. Intell. Robots Syst. (IROS)*, Sep. 2015, pp. 5512–5517.

[205] W. Sun, L. G. Torres, J. Van Den Berg, and R. Alterovitz, "Safe motion planning for imprecise robotic manipulators by minimizing probability of collision," in *Robotics Research*. Cham, Switzerland: Springer, 2016, pp. 685–701.

[206] Y. Chen, Z. Li, W. Xu, Y. Wang, and H. Ren, "Minimum sweeping area motion planning for flexible serpentine surgical manipulator with kinematic constraints," in *Proc. IEEE/RSJ Int. Conf. Intell. Robots Syst. (IROS)*, Sep. 2015, pp. 6348–6353.

[207] J. Granna, A. Nabavi, and J. Burgner-Kahrs, "Computer-assisted planning for a concentric tube robotic system in neurosurgery," *Int. J. Comput. Assist. Radiol. Surg.*, vol. 14, no. 2, pp. 335–344, Feb. 2019.

ABOUT THE AUTHORS

Pierre E. Dupont (Fellow, IEEE) received the B.S., M.S., and Ph.D. degrees in mechanical engineering from Rensselaer Polytechnic Institute, Troy, NY, USA, in 1982, 1984, and 1988, respectively.

From 1988 to 1990, he was a Postdoctoral Fellow with the School of Engineering and Applied Sciences, Harvard University, Cambridge, MA, USA. He was a Professor of mechanical engineering and biomedical engineering with Boston University, Boston, MA, USA. He is currently the Chief of pediatric cardiac bioengineering and the holder of the Edward P. Marram Chair at Boston Children's Hospital, Harvard Medical School, Boston, MA, USA. He is also a Professor of surgery with the Harvard Medical School. His research group develops robotic instrumentation and imaging technology for medical applications.

Dr. Dupont is also a member of the Advisory Board for Science Robotics. He just completed a five-year term as a Senior Editor for the IEEE TRANSACTIONS ON ROBOTICS.

Nabil Simaan (Fellow, IEEE) received the Ph.D. degree in mechanical engineering from the Technion—Israel Institute of Technology, Haifa, Israel, in 2002.

In 2003, he was a Postdoctoral Research Scientist with Johns Hopkins University National Science Foundation (NSF) ERC-CISST, Baltimore, MD, USA. In 2005, he joined Columbia University, New York, NY, USA. In fall 2010, he joined Vanderbilt University, Nashville, TN, USA. His research interests include medical robotics, kinematics, robot modeling and control, and human–robot interaction.

Dr. Simaan was named an IEEE Fellow in 2020 and an ASME Fellow in 2021 for contributions to dexterous continuum robotics. In 2009, he received the NSF Career Award for young investigators to design new algorithms and robots for safe interaction with the anatomy.

Howie Choset (Fellow, IEEE) received the B.S. degree in computer science and the B.S. degree in economics from the University of Pennsylvania, Philadelphia, PA, USA, in 1990, and the M.S. and Ph.D. degrees in mechanical engineering from the California Institute of Technology, Pasadena, CA, USA, in 1991 and 1996, respectively.

He joined Carnegie Mellon, Pittsburgh, PA, USA, in 1996, where his group conducts research in medical robotics, manufacturing, search and rescue, and recycling. In 2017, he cofounded the Advanced Robotics for Manufacturing Institute, Pittsburgh.

Dr. Choset was named an IEEE Fellow for contributions to snake robots, multiagent systems, and estimation of continuum robots in 2015. This work was recognized by the Engelberger Award in 2019.

Caleb Rucker (Member, IEEE) received the B.S. degree in engineering mechanics and mathematics from Lipscomb University, Nashville, TN, USA, in 2006, and the Ph.D. degree in mechanical engineering from Vanderbilt University, Nashville, in 2010.

From 2011 to 2013, he was a Postdoctoral Fellow in biomedical engineering with Vanderbilt University. He is currently an Associate Professor of mechanical engineering with The University of Tennessee, Knoxville, TN, USA, where he directs the Robotics, Engineering, and Continuum Mechanics in Healthcare Laboratory (REACH Lab).

Dr. Rucker received the NSF CAREER Award in 2017.